ESD-TR-79-325

LEVEL III

AD A089822

1

Solid State Research

1980

DTIC
ELECTE
OCT 2 1980
S   D
B

80 10 2 049

This technical report has been reviewed and is approved for publication.

FOR THE COMMANDER

Joseph C. Syiek

Joseph C. Syiek
Project Officer
Lincoln Laboratory Project Office

MASSACHUSETTS INSTITUTE OF TECHNOLOGY

LINCOLN LABORATORY

SOLID STATE RESEARCH

QUARTERLY TECHNICAL SUMMARY REPORT

1 NOVEMBER 1979 – 31 JANUARY 1980

ISSUED 24 JUNE 1980

LEXINGTON   MASSACHUSETTS

ABSTRACT

This report covers in detail the solid state research work of the Solid
State Division at Lincoln Laboratory for the period 1 November 1979
through 31 January 1930. The topics covered are Solid State Device
Research, Quantum Electronics, Materials Research, Microelec-
tronics, and Analog Device Technology. Funding is primarily pro-
vided by the Air Force, with additional support provided by the Army,
DARPA, Navy, NASA, NSF, and DOE.

Accession For		
NTIS GRA&I	☑	
DTIC TAB	☐	
Unannounced	☐	
Justification		
By		
Distribution/		
Availability Codes		
Dist	Avail and/or Special	
A		

CONTENTS

INTRODUCTION

I. SOLID STATE DEVICE RESEARCH

Substantial reduction in the surface component of the dark current in GaInAsP/InP avalanche photodiodes has been achieved by the application of new surface passivation techniques. Leakage current densities as low as 4×10^{-6} A/cm^2 at half the breakdown voltage have been achieved.

CW operation at temperatures up to 55°C has been achieved for GaInAsP/InP double-heterostructure (DH) lasers emitting at 1.5 μm, which were grown without a GaInAsP buffer layer. These devices are of interest for use as sources in fiber optics communications systems, since the lowest transmission loss reported for fused-silica optical fibers occurs at 1.55 μm.

The electrical characteristics of InP ion implanted with Sn, Ge, Si, and C have been investigated. All of these column-IV elements yielded n-type conductivity and Sn, Ge, and Si showed high electrical activation; however, implanted C was found to have a net electrical activation of only about 5 percent.

The growth-temperature dependence of the GaInAsP/InP lattice mismatch has been measured over a wide range of quaternary compositions. Smooth GaInAsP layers have been grown directly on InP substrates without an InP buffer layer; however, the use of an InP layer results in a smooth GaInAsP/InP interface, which is needed for DH lasers.

II. QUANTUM ELECTRONICS

Fluorescence lifetime and fluorescence spectra have been studied for several transition metal systems in which laser action either has been obtained or may be possible. The results of lifetime vs temperature measurements indicate the potential for room-temperature laser operation in $Ni:CaY_2Mg_2Ge_3O_{12}$ (CAMGAR) and the limitation of lasing in $V:MgF_2$ to below 200 K.

Schottky diode mixer operation has been demonstrated at 30-THz carrier frequencies. Using isotopic CO_2 lasers, beats were observed to 15.6 GHz. Experiments are under way at higher frequencies which should further clarify the mixing mechanism.

III. MATERIALS RESEARCH

Conversion efficiencies exceeding 13 percent at AM1 and open-circuit voltages approaching 0.9 V have been achieved for GaAs homojunction solar cells grown by chemical vapor deposition on large-grained GaAs substrates. These values, the highest so far reported for polycrystalline GaAs cells, were obtained by using a new passivation method that involves electroplating Sn on the GaAs surface and subsequent heat treatment.

Homojunction InP solar cells with conversion efficiencies up to 15 percent at AM1, the highest values reported for InP cells of any type, have been fabricated on single-crystal InP substrates. The cells incorporate an $n^+/p/p^+$ structure prepared by liquid-phase epitaxy and an antireflection coating formed by anodic oxidation of the n^+ surface.

With the objective of developing a method for preparing low-cost Ge substrates for GaAs solar cells, an optical transmission technique has been used to measure the crystallization front velocity during scanned laser crystallization of amorphous Ge films. The measured velocities range from 146 to 260 cm/sec, compared with the laser scanning velocity of 0.5 cm/sec.

IV. MICROELECTRONICS

Quantitative measurements have been made of the orientation, texture, and sheet re-sistivity of silicon films grown by graphoepitaxy on fused-silica substrates. On 3.8-μm spatial-period surface gratings the [100] directions are parallel to the grating to within $\pm15°$ and perpendicular to the substrate surface to within $\pm1.5°$. The sheet resistivity of silicon films 0.5-um thick doped with phosphorus was 2.5 times larger than that measured for silicon wafers with similar doping used for controls.

The mixing action in a SAW accumulating correlator with CCD readout has been deter-mined to occur in the varactor-like nonlinearity of the drain region of the sampling-finger bias transistors. The accumulation of the mixing product takes place in an RC integrator formed by the resistance of the nearly pinched-off transfer channel and the capacitance of the CCD φ_1 well.

A multiplying digital-to-analog converter of novel design, which uses capacitance-weighted CCD inputs, has been implemented using buried-channel CCD techniques. The device has been used to D/A convert 8-bit words at a 10-MHz digital-word data rate. The device can be integrated on-chip with CCD signal-processing devices and will accept digital inputs directly from a TTL source with no TTL-to-MOS buffer.

Two-phase GaAs CCDs have been fabricated which utilize an etched step to create the necessary potential barrier under each gate. Shadow evaporation is used to form sub-micrometer gaps between the electrodes without photolithography. The CCDs ex-hibited 0.993 transfer efficiencies with uniphase clocking at frequencies up to 10 MHz.

The underlying physical events which govern transport properties in devices operated at high frequencies or with submicrometer dimensions have been identified and for-mulated for use in device modeling. For devices where the basic frequency limita-tions are RC in nature, a high mobility and hence long momentum-relaxation time is required. However, in transferred electron and IMPATT devices the high-frequency performance will be enhanced when the energy relaxation time is short, which implies lower mobility.

V. ANALOG DEVICE TECHNOLOGY

A satellite-borne chirp-Fourier-transform system for efficient demodulation of frequency-shift-keyed uplink signals has been developed. This system exploits the capabilities of four SAW reflective-array compressors to implement a pair of convolve-multiply-convolve chirp-transform circuits which are compact and low-power. The system allows the continuous demodulation of high-data-rate communications from 100 simultaneous users with a minimum of intersymbol interference.

The performance of gap-coupled acoustoelectric convolvers has been extended to 200-MHz bandwidth and 2400 time-bandwidth product. This structure is very rugged, as has recently been demonstrated by an extensive series of shock and vibration tests. Projections are made of the limits to which matched filter performance may be extended with this convolver technology.

REPORTS ON SOLID STATE RESEARCH

15 November 1979 through 15 February 1980

PUBLISHED REPORTS

Journal Articles

JA No.

4871	MBE Techniques for IV-VI Optoelectronic Devices	H. Holloway[*] J. N. Walpole	Prog. Cryst. Growth & Charact. 2, 49 (1979)
4895	Extended Measurement and Analysis of the ν_3 Infrared Band of Methane	D. L. Gray[*] A. G. Robiette[*] A. S. Pine	J. Mol. Spectrosc. 77, 440 (1979)
4932	Electron Paramagnetic Resonance in Ferrous Fluosilicate at Submillimeter Wavelengths	R. S. Rubins[*] H. R. Fetterman	J. Chem. Phys. 71, 5163 (1979)
4934	Calculated and Measured Efficiencies of Thin-Film Shallow-Homojunction GaAs Solar Cells on Ge Substrates	J. C. C. Fan C. O. Bozler B. J. Palm	Appl. Phys. Lett. 35, 875 (1979)
4935	The Excimer Laser: A New Ultraviolet Source for Medical, Biological, and Chemical Applications	R. M. Osgood, Jr.	In Laser Applications in Medicine and Biology (Plenum Press, New York, 1979)
4960	Efficient Infrared ac Kerr Switches Using Simple Cryogenic Liquids	S. R. J. Brueck H. Kildal	Appl. Phys. Lett. 35, 665 (1979)
4973	Tunable Submillimeter Sources Applied to the Excited State Rotational Spectroscopy and Kinetics of CH_3F	W. A. Blumberg H. R. Fetterman D. D. Peck P. F. Goldsmith[*]	Appl. Phys. Lett. 35, 582 (1979)
4978	Subtraction of Signal Overlaps in Rutherford Backscattering Spectrometry	Z. L. Liau	Appl. Phys. Lett. 36, 51 (1980)
4986	R-Branch Head of the ν_3 Band of CO_2 at Elevated Temperatures	A. S. Pine G. Guelachvili[*]	J. Mol. Spectrosc. 79, 84 (1980)
4987	Broadly Tunable cw Operation of $Ni:MgF_2$ and $CO \cdot MgF_2$ Lasers	P. F. Moulton A. Mooradian	Appl. Phys. Lett. 35, 838 (1979)
5000	Replication of 175 Å Lines and Spaces in PMMA by X-Ray Lithography	D. C. Flanders	Appl. Phys. Lett. 36, 1 (1980)

[*] Author not at Lincoln Laboratory.

5003	Stimulated Level Shifting and Velocity Inversion in UV-Laser-Excited Photofragments	D. J. Ehrlich R. M. Osgood, Jr.	In Laser Spectroscopy IV, H. Walther and K.W. Rothe, Eds. (Springer-Verlag, Heidelberg, 1979), p.629
5004	Atomic-Transition Lasers Based on Two-Photon Dissociation of Metal-Triiodide Vapors	T. F. Deutsch D. J. Ehrlich R. M. Osgood, Jr.	Opt. Lett. **4**, 378 (1979)
5012	High-Speed InP Optoelectronic Switch	F. J. Leonberger P. F. Moulton	Appl. Phys. Lett. **35**, 712 (1979)
5023	Efficient Shallow-Homojunction GaAs Solar Cells by Molecular Beam Epitaxy	J. C. C. Fan A. R. Calawa R. L. Chapman G. W. Turner	Appl. Phys. Lett. **35**, 804 (1979)
5028	Interband Magnetoabsorption of $In_{0.53}Ga_{0.47}As$	K. Alavi[*] R. L. Aggarwal[*] S. H. Groves	Phys. Rev. B **21**, 1311 (1980)

Meeting Speeches

4949	Effect of Pressure and Composition on Fast Na^+-Ion Transport in the System $Na_{1+x}Zr_2Si_xP_{3-x}O_{12}$	J. A. Kafalas R. J. Cava[*]	In Proceedings of the 1979 International Conference on Fast Ion Transport in Solids (Elsevier North-Holland, New York, 1979), pp.419, 431, and 479
4986	Crystal Structure and Ionic Conductivity of a New Superionic Conductor, $Na_3Sc_2P_3O_{12}$	H. Y-P. Hong	
4996	Analysis of the Alternating Current Properties of LISICON Ceramics	M. L. Bayard	
5028	Tunable Transition-Metal-Doped Solid State Lasers	P. F. Moulton A. Mooradian	In Laser Spectroscopy IV, H. Walther and K.W. Rothe, Eds. (Springer-Verlag, Heidelberg, 1979), p.584
5053	Wideband SAW Fourier-Transform-Processor Design and Applications	R. C. Williamson	Case Studies in Advanced Signal Processing (IEE, London, 1979), Vol.180, pp.236-243
5095	Fabrication of Submicrometer Period Gratings with Precisely Defined Profiles for Integrated Optics Applications	D. C. Flanders A. M. Hawryluk	Integrated and Guided-Wave Optics Technical Digest (January 1980), Session WA3-1
5216	Microfabrication for Guided-Wave Optical Devices	H. I. Smith	Integrated and Guided Wave Optics Technical Digest (January 1980), Session WA1-1

[*] Author not at Lincoln Laboratory.

UNPUBLISHED REPORTS

Journal Articles

Meeting Speeches[†]

---

* Author not at Lincoln Laboratory.

[†] Titles of Meeting Speeches are listed for information only. No copies are available for distribution.

---

* Author not at Lincoln Laboratory.

*Author not at Lincoln Laboratory.

---

*Author not at Lincoln Laboratory.

ORGANIZATION

SOLID STATE DIVISION

A. L. McWhorter, *Head*
I. Melngailis, *Associate Head*
J. F. Goodwin, *Assistant*

R. H. Rediker, *Senior Staff*
P. E. Tannenwald, *Senior Staff*

QUANTUM ELECTRONICS

A. Mooradian, *Leader*
P. L. Kelley, *Associate Leader*

Barch, W. E.	Fetterman, H. R.
Belanger, L. J.	Fleming, M. W.*
Blumberg, W. A. M.	Hancock, R. C.
Brueck, S. R. J.	Kildal, H.
Burke, J. W.	Killinger, D. K.
Bushee, J. F., Jr.	Menyuk, N.
Chinn, S. R.	Moulton, P. F.
DeFeo, W. E.	Osgood, R. M., Jr.
Deutsch, T. F.	Parker, C. D.
Ehrlich, D. J.	Peck, D. D.
Feldman, B.	Pine, A. S.

ELECTRONIC MATERIALS

A. J. Strauss, *Leader*
H. J. Zeiger, *Associate Leader*
J. G. Mavroides, *Senior Staff*

Anderson, C. H., Jr.	Hsieh, J. J.
Button, M. J.	Iseler, G. W.
Chapman, R. L.	Kafalas, J. A.
Davis, F. M.	Kolesar, D. F.
Delaney, E. J.	Krohn, L., Jr.
Fahey, R. E.	Mastromattei, E. L.
Fan, J. C. C.	Owens, E. B.
Finn, M. C.	Palm, B. J.
Flutie, R. E.	Pantano, J. V.
Foley, G. H.	Salerno, J. P.*
Gale, R. P.	Tracy, D. M.
Hong, H. Y-P.	Vohl, P.

APPLIED PHYSICS

R. C. Williamson, *Leader*
C. E. Hurwitz, *Associate Leader*
T. C. Harman, *Senior Staff*
R. H. Kingston, *Senior Staff*

Armiento, C. A.*	Leonberger, F. J.
Calawa, A. R.	Liau, Z-L.
Carter, F. B.	Lind, T. A.
DeMeo, N. L., Jr.	McBride, W. F.
Diadiuk, V.	Paladino, A. E.
Donnelly, J. P.	Plonko, M. C.
Duffy, P. E.	Spears, D. L.
Ferrante, G. A.	Tsang, D. Z.*
Foyt, A. G.	Turner, G. W.
Groves, S. H.	Walpole, J. N.
Kirsch, S. T.*	

ANALOG DEVICE TECHNOLOGY

E. Stern, *Leader*
J. H. Cafarella, *Assistant Leader*
R. W. Ralston, *Assistant Leader*

Anderson, A. C.	Kernan, W. C.
Arsenault, D. R.	Leung, I.
Baker, R. P.	Lynch, J. T.
Becker, R. A.	Oates, D. E.
Behrmann, G. J.	Reible, S. A.
Brogan, W. T.	Slattery, R. L.
Dolat, V. S.	Withers, R. S.
Holtham, J. H.	Yao, I.

MICROELECTRONICS

W. T. Lindley, *Leader*
F. J. Bachner, *Associate Leader*
H. I. Smith, *Assistant Leader*

Alley, G. D.	Felton, B. J.	McGonagle, W. H.
Baker, F-M.	Flanders, D. C.	Melngailis, J.
Bozler, C. O.	Geis, M. W.	Mountain, R. W.
Burke, B. E.	Gray, R. V.	Murphy, R. A.
Chiang, A. M.	Hansell, G. L.*	Nichols, K. H.
Chu, A.	Hawryluk, A. M.*	Piacentini, W. J.
Clifton, B. J.	Jacobsen, E. H.	Pichler, H. H.
Daniels, P. J.	Lau, C-L.*	Rathman, D. D.
DeGraff, P. D.	Lincoln, G. A., Jr.	Shaver, D. C.†
Durant, G. L.	Lyszczarz, T.	Silversmith, D. J.
Economou, N. P.	Macropoulos, W.	Smythe, D. L., Jr.
Efremow, N., Jr	Mahoney, L. J.	Sotomayor-Diaz, O.†
Elta, M. E.	McClelland, R. W.	Wilde, R. E.

---

*Research Assistant
†Staff Associate

xvi

I. SOLID STATE DEVICE RESEARCH

A. SURFACE PASSIVATION OF GaInAsP/InP AVALANCHE PHOTODIODES

Substantial reduction in the surface component of the dark current in GaInAsP/InP avalanche photodiodes has been achieved by the application of new surface passivation techniques. Two previously described mesa structures were investigated, one with the p-n junction located in the GaInAsP (Ref. 1) and the other with the p-n junction in the InP but the carrier generation taking place in the GaInAsP (Ref. 2). Different techniques were found to be optimum for each structure.

Since Si_3N_4 has been used successfully to passivate p^+ InP avalanche photodiodes,[3] a Si_3N_4 film, ~900 Å thick, was initially used[1] as passivation for the devices with the junction in the InP. Reasonably low leakage current densities (~3×10^{-5} A/cm^2 at 1/2 V_b is the breakdown voltage) could be obtained this way; however, a marked degradation in device performance was observed when the devices were exposed to high humidity or sustained high bias (~0.9 V_b for ~1 min.). The sensitivity to atmospheric moisture could be reduced simply by adding a layer of fully cured photoresist (PR) to the Si_3N_4-covered devices. The marked increase in leakage current (sometimes as high as 30 percent) observed with sustained bias, on the other hand, was not eliminated and made it necessary to investigate other passivation schemes. The most successful of these was the application of a polyimide (PI) film* (5 to 8 μm thick) directly over the freshly etched mesas. The PI film was deposited and patterned using standard photolithographic techniques and was imidized by baking at 120° and 200°C for 1 hr each. Further baking or higher temperatures resulted in degraded device characteristics, possibly due to impurity diffusion. When the above procedures were used, the PI-passivated devices exhibited no current increase with sustained bias. Leakage current densities as low as 3×10^{-7} A/cm^2 at 1/2 V_b were observed.

Devices of the second type, with the p-n junction in the GaInAsP layer, exhibited high leakage currents not only when uncoated, but also when passivated with Si_3N_4 or PI. The surface-related nature of the leakage currents was confirmed by testing the uncoated devices in several gaseous environments (O_2, NH_4OH, SF_6). In particular, when tested in an SF_6 atmosphere,[4] the devices showed a dramatic improvement in performance, exhibiting low leakage current and sharp breakdown. This might be attributed to the high electron affinity of SF_6, which helps reduce excess surface charge, and to its high dielectric constant, which helps prevent fringing fields at the exposed junction. Unfortunately these effects disappeared when the device was removed from the SF_6 ambient.

In a separate experiment it had been observed that when PR was applied immediately after etching the mesas, the device characteristics were similar to those exhibited in the SF_6 atmosphere. Based upon these two observations, a method was developed in which SF_6 was used as the propellant gas for PR spraying, producing a surface coating that combines all the advantages of the PR passivation with those of the SF_6 ambient, but permits the operation of the device in air. Devices passivated in this manner exhibited current densities as low as ~4×10^{-6} A/cm^2 at 1/2 V_b. Figure I-1 shows the reverse I-V characteristics of a device before and after passivation with SF_6-propelled PR. The passivation effects were reversible upon removal and

---

* DuPont PI-255 polyimide coating for semiconductor fabrication.

UPPER TRACE:
   x SCALE: 10 V/div
   y SCALE: 20 μA/div

LOWER TRACE:
   x SCALE: 10 V/div
   y SCALE: 2 μA/div

COMMON ORIGIN
FOR BOTH CURVES
IS INDICATED

(a)

UPPER TRACE:
   x SCALE: 10 V/div
   y SCALE: 20 μA/div

LOWER TRACE:
   x SCALE: 10 V/div
   y SCALE: 1 μA/div

ORIGIN OF EACH CURVE
IS INDICATED

(b)

-8-16797-1
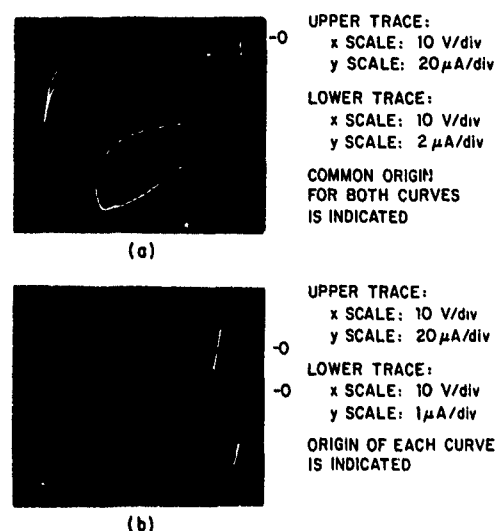
Fig. I-1. Reverse I-V characteristics for p^+-InP/n-Q n^+-InP: (a) before SF_6-propelled PR passivation; (b) after SF_6-propelled PR passivation.

reapplication of the SF_6-propelled PR layer. The presence of the PR layer was found to have no adverse effect on the photoresponse of these devices.

V. Diadiuk
S. H. Groves
C. E. Hurwitz

B. HIGH-TEMPERATURE CW OPERATION OF GaInAsP/InP LASERS EMITTING AT 1.5 μm

The lowest transmission loss reported[5] for fused-silica optical fibers, 0.2 dB/km, has been obtained at 1.55 μm where the material dispersion is still low enough for wide-bandwidth operation. Consequently, there is strong current interest in the development of diode lasers emitting at ~1.5 μm for use as sources in fiber-optics communications systems. In this section we report the fabrication of GaInAsP/InP double-heterostructure (DH) lasers emitting in this wavelength region that have been operated CW at heat-sink temperatures as high as 55°C. Although room-temperature CW operation of 1.5-μm GaInAsP/InP lasers has been described recently,[6-9] CW operation of these devices at temperatures above 20°C has not been reported. The high-temperature capability of the present lasers is significant not only because it would permit system operation above room temperature if desirable, but also because longer lifetimes for room-temperature operation can be expected for devices with this capability. For the laser with the best room-temperature characteristics, the CW threshold current I_{th} was 120 mA and the external differential quantum efficiency η_d was 28 percent. These values are comparable to those obtained for GaInAsP/InP DH lasers emitting at 1.1 to 1.3 μm (Ref. 10) and significantly better than the best room-temperature values (I_{th} = 150 mA, η_d = 19 percent) previously obtained[8] for 1.5-μm devices.

The heterostructures used for conventional GaInAsP/InP DH lasers emitting at 1.1 to 1.3 μm consist of successive InP, GaInAsP, and InP layers grown by liquid-phase epitaxy (LPE) at

2

630° to 650°C on InP substrates. The thickness of the GaInAsP active layer is of the order of 0.1 μm. Considerable difficulty is encountered in using the same structure and growth procedure for 1.5-μm lasers because the P content in the thin active layer is so low that there is a strong tendency for this layer to be dissolved by the growth solution used for deposition of the upper InP layer. In fabricating the 1.5-μm lasers reported previously, the dissolution problem was solved either by lowering the LPE growth temperature for the upper InP layer to 592°C (Ref. 6) in order to reduce the solubility of the active layer in the InP growth solution, or by growing a GaInAsP buffer layer between the active layer and the upper InP layer, using an intermediate composition for the buffer layer such that its growth solution did not dissolve the active layer[7-9] Neither of these methods was employed in preparing the lasers described here. Instead, conventional three-layer heterostructures were obtained by LPE growth at 640°C (Ref. 11), but dissolution was prevented by supercooling the growth solution for the upper InP layer by 10° to 12°C before placing it in contact with the active layer.

We have used Auger spectroscopy in combination with ion-beam sputtering to analyze one of the heterostructures grown by the supercooling technique. The approximately 0.4-μm-thick active layer was found to have a symmetrical composition profile, with a central region of uniform composition bordered at the top and bottom by transition regions each about 0.05 μm thick in which the composition changed gradually to that of InP. The dependence of composition on distance was similar in these two regions. Since dissolution of the lower InP layer does not occur during the growth of the GaInAsP active layer, the similarity in the composition gradients indicates that dissolution of the active layer did not occur during growth of the upper InP layer.

The CW lasers were fabricated from heterostructures in which all three epitaxial layers were n-type, and stripes were defined by the deep-Zn-diffusion technique used previously for shorter-wavelength devices.[10] Figure I-2 shows the curves of light output vs current measured for CW operation of one laser at 20°, 30°, 40°, and 50°C. At 20°C, where the emission wavelength was 1.51 μm, I_{th} = 150 mA and η_d = 13 percent. For this device, I_{th} is approximately proportional to $\exp[-T/T_o]$, with T_o = 53°C near room temperature, in good agreement with previous results for pulsed operation.[8] The maximum CW operating temperature was 55°C, the highest value we have achieved for 1.5-μm lasers.

Figure I-3 shows the emission spectra obtained for 20° and 40°C operation of another CW laser at about 20 percent above threshold. The emission peak moves from 1.506 Å at 20°C to 1.517 Å at 40°C, a shift of 5.5 Å/deg. Figure I-4 shows the emission spectrum obtained for 22°C operation of a third laser at 17 percent above threshold, where the emission peak occurs at 1.559 μm. The lasers of Figs. I-3 and -4 were fabricated from two different wafers. The composition of the growth solution for the active layer was the same in both cases, but the active layer thicknesses were 0.1 and 0.4 μm, respectively.

For all the CW lasers tested, a single longitudinal mode was predominant, as shown by the spectra of Figs. I-3 and -4. Figure I-5 shows the far-field patterns as a function of current for a second laser fabricated from the same wafer as the device of Fig. I-3. These patterns show single transverse mode operation up to the highest current used, about 70 percent above threshold, where the output exceeded 10 mW/facet.

In addition to characterizing the CW operation of stripe-geometry lasers, we have also investigated the pulsed operation of broad-area 1.5-μm lasers, which were fabricated from wafers with an as-grown p-type InP top layer. The values of threshold current density J_{th} are comparable to those broad-area lasers emitting at 1.1 to 1.3 μm (Ref. 12). The best value of J_{th},
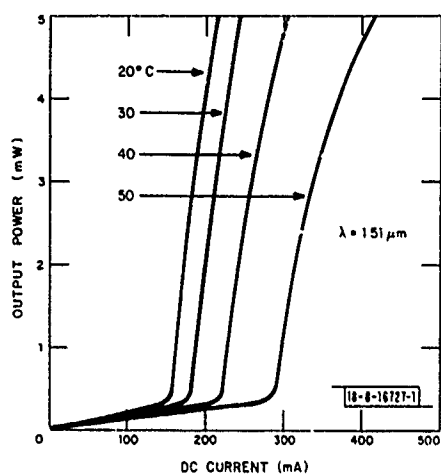
Fig. I-2. Light output vs current for CW operation of GaInAsP/InP laser emitting at 1.51 μm.
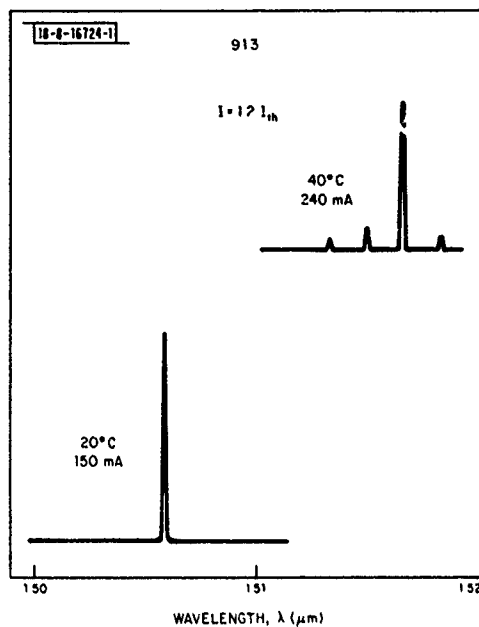
Fig. I-3. Emission spectra for GaInAsP/InP laser at 20° and 40°C.
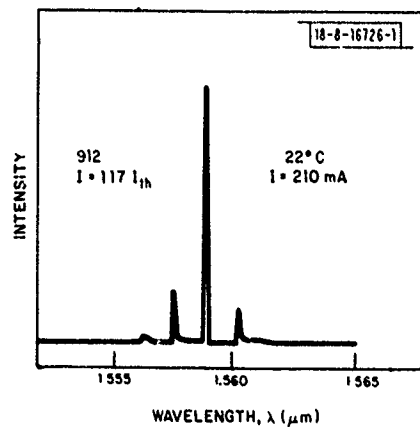
Fig. I-4. Emission spectrum for GaInAsP/InP laser at 22°C.
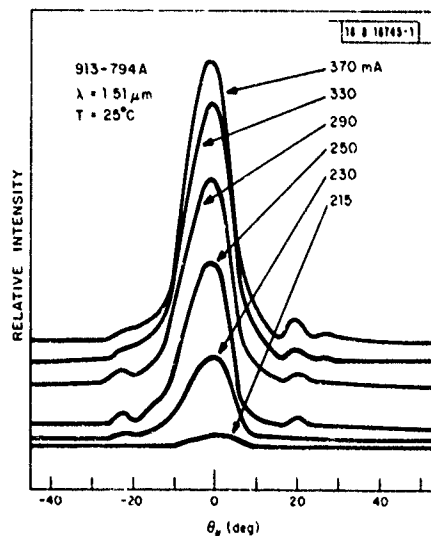
Fig. I-5. Far-field patterns as a function of current for GaInAsP/InP laser emitting at 1.51 μm.

4

1.7 kA/cm^2, normalized to a cavity length of 250 μm, is the lowest value so far reported for 1.5-μm lasers. For diodes from substantial areas of each wafer, however, laser action did not occur even at current densities up to 20 kA/cm^2. This inhomogeneity suggests that at least partial dissolution of the active layer may have occurred in those areas which did not yield laser diodes.

<div style="text-align: right">J. J. Hsieh</div>

C. ELECTRICAL CHARACTERISTICS OF InP IMPLANTED WITH COLUMN IV ELEMENTS

Ion implantation in InP has been receiving an increasing amount of attention recently because of its applicability to the fabrication of microwave and electrooptic devices. Previously, work[2,13-18] has dealt primarily with InP implanted with column II or column VI elements, whereas among the column IV elements, only Si has been investigated to any extent.[2,13,14,17,18] In this section we report results of a study on the electrical characteristics of InP implanted with the column IV elements from C to Sn, including new and more detailed data for Si in InP.

High-resistivity ($\rho \geq 10^7$ Ω-cm), Fe-doped, (111)-oriented InP samples were used in these experiments. Following implantation, the samples were annealed at 750°C for 10 to 15 min. using a PSG (phosphosilicate glass) encapsulation technique described previously.[2,13] Details of the sample processing before and after implantation can be found in Refs. 2, 13, and 16.

The sheet carrier concentrations and mobilities of InP samples implanted with 1×10^{14} cm^{-2} of 400-keV C, Si, Ge, and Sn are shown in Fig. I-6 as a function of implant temperature. Implantation of all these column IV elements resulted in layers showing n-type conductivity. As shown in Fig. I-6(a), however, data from the samples implanted with C indicate a low net electrical activation (about 5 percent) of the implanted C. Samples implanted with carbon doses ranging from 1×10^{13} cm^{-2} to 1×10^{15} cm^{-2} all show this same effect. These results indicate that C is likely highly amphoteric in InP, although other possibilities, such as the location of most of the carbon on interstitial sites, cannot be entirely ruled out. This behavior of implanted C in InP contrasts with that in GaAs, where implanted C was found to be p-type with up to 50 percent effective doping efficiency.[19]

Samples implanted with the other column IV elements, Si, Ge, and Sn, all showed n-type behavior with good electrical activation and a similar dependence on implantation temperature and dose. For these elements, sheet resistivities of InP samples implanted at temperatures of 150 to 200°C were generally lower than those of samples implanted at room temperature. The sheet mobilities were always higher for the elevated temperature implants, but several anomalies in the sheet carrier concentration as a function of implant temperature and dose were observed.

The results for 1×10^{14} cm^{-2} silicon implants are shown in Fig. I-6(b). Over the 25° to 200°C range of sample temperature during implantation, the sheet carrier concentration and mobility increased with increasing implant temperature. As indicated in the figure, there is considerable scatter in the room-temperature results with the measured sheet carrier concentrations ranging from 4.8×10^{13} to 7.0×10^{13} cm^{-2}. The room-temperature implanted samples with the higher sheet concentrations invariably had lower mobilities, so that even when the sheet concentrations were comparable to those on samples implanted at elevated temperatures, the sheet resistivities were always considerably higher. Since residual implant damage in InP has been shown to result in n-type conductivity with low mobility,[2,13] the variability of these room-temperature implant results indicate that Si is of an intermediate mass between light ions and
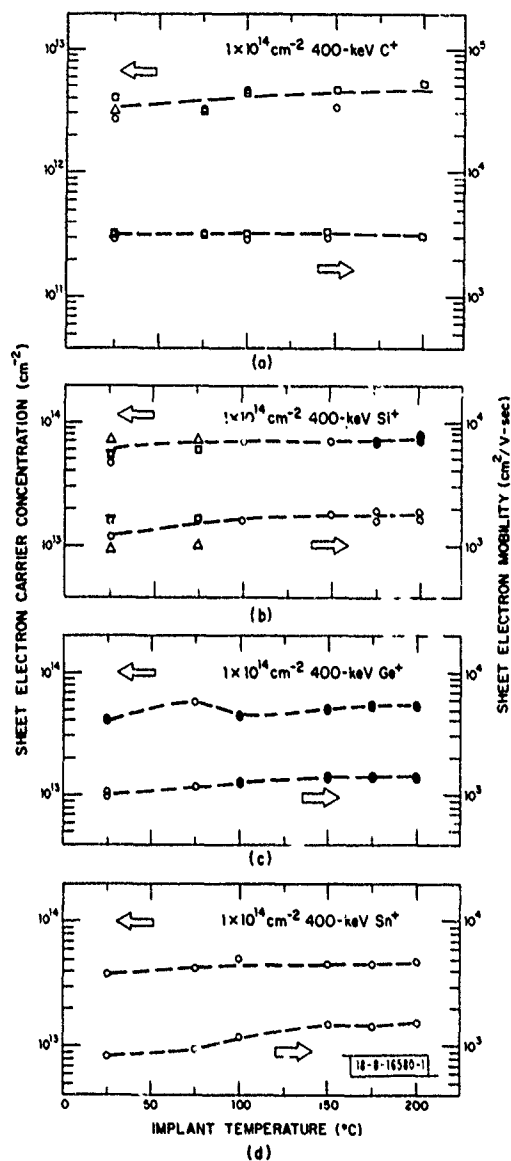
Fig. I-6. The sheet carrier concentration and mobilities vs implant temperature of InP samples implanted with 1×10^{14} cm^{-2} of 400 keV: (a) C, (b) Si, (c) Ge, and (d) Sn. All the samples were annealed at 750°C using a PSG encapsulation technique.

heavy ions and that the damage created during room-temperature Si implantation into InP is critically dependent on the precise implant parameters.[20] The results on samples implanted with silicon at elevated temperatures were very reproducible. All samples implanted at 200°C with 1×10^{14} cm^{-2} had measured sheet carrier concentrations and mobilities in the range (7.6 to 7.8) $\times 10^3$ cm^{-2} and (1800 to 2000) cm^2/V-sec, respectively.

For 1×10^{14} cm^{-2} germanium implants, the results on samples implanted at all temperatures were reproducible. As shown in Fig. I-6(c), higher sheet mobilities were obtained on the sample implanted at 150° to 200°C. The sheet carrier concentrations measured on these samples were also higher than those obtained on similar samples implanted at room temperature, but as shown in the figure, there is an unexpected but reproducible anomalous peak in the sheet concentration for samples implanted at 75°C. The mobility measured on these samples (1100 to 1200 cm^2/V-sec), however, were sufficiently lower than on those implanted at 150° to 200°C, so that the higher-temperature implanted samples invariably had lower sheet resistivities. All the samples implanted at temperatures of 150° to 200°C with 1×10^{14} cm^{-2} of Ge exhibited measured sheet carrier concentrations and mobilities in the ranges (5.2 to 5.6) $\times 10^{13}$ cm^{-2} and (1480 to 1540) cm^2/V-sec, respectively.

Samples implanted with 1×10^{14} cm^{-2} of 400-keV Sn are shown in Fig. I-6(d). They are very similar to those obtained with Ge, except for the absence of the pronounced maximum in sheet carrier concentration. For samples implanted at 200°C, the measured sheet carrier concentrations and mobilities were typically 4.6×10^{13} cm^{-2} and 1450 cm^2/V-sec, respectively.

In contrast to the results discussed above, for Si, Ge, or Sn doses higher than about mid-10^{14} cm^{-2}, the sheet carrier concentrations measured on samples implanted at room temperature were higher than those measured on samples implanted at 150° to 200°C. This is illustrated in Fig. I-7, where the sheet electron concentration and mobility vs dose for InP
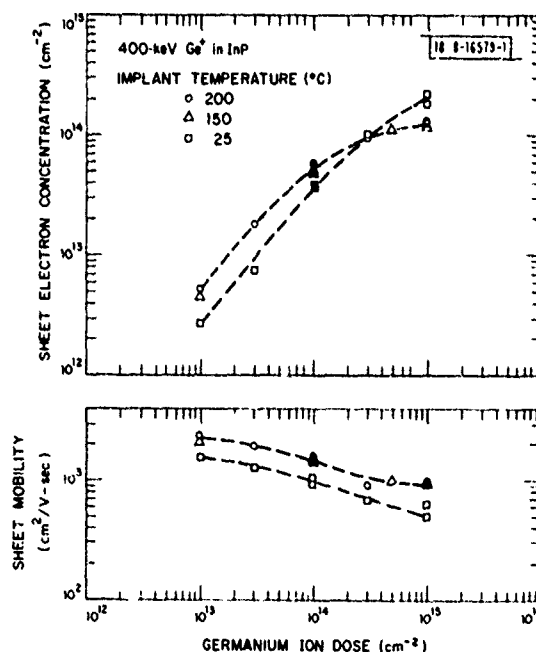
Fig. I-7. The sheet carrier concentrations and mobilities vs dose of InP samples implanted with 400-keV Ge at several temperatures, from room temperature to 200°C.

samples implanted with 400-keV Ge$^+$ at several temperatures between room temperature and 200°C are plotted. For doses less than 10^{14} cm^{-2}, the sheet carrier concentration and mobility vary qualitatively with implant temperature as indicated in Fig. I-6. For doses of 3×10^{14} cm^{-2}, the measured sheet carrier concentrations are essentially equal for samples implanted at room temperature and 200°C, while for doses of 1×10^{15} cm^{-2} the concentrations in the samples implanted at room temperature [$(1.8$ to $2.2) \times 10^{13}$ cm^{-2}] were higher than those measured on samples implanted at 150° and 200°C [$(1.2$ to $1.3) \times 10^{14}$ cm^{-2}]. The sheet mobilities, however, are considerably higher on the samples implanted at elevated temperatures so that the sheet resistivities of all the samples implanted with 1×10^{15} cm^{-2} are about 55 Ω/□.

Similar behavior at high doses also has been observed with Si and Sn. For 400-keV Si doses of 1×10^{15} cm^{-2}, samples implanted at room temperature had sheet carrier concentrations and mobilities of about 4.0×10^{14} cm^{-2} and 780 cm^2/V-sec for a sheet resistivity of 20 Ω/□. Similar samples implanted at 200°C had sheet concentrations, mobilities, and resistivities of 2.8×10^{14} cm^{-2}, 1500 cm^2/V-sec, and 15 Ω/□, respectively.

To examine the effects of implant temperature and dose on the spatial distribution of the electrical active implanted ions, several samples were selected for depth profiling using a series of Hall measurements combined with step etching.[21] Figure I-8 shows the carrier
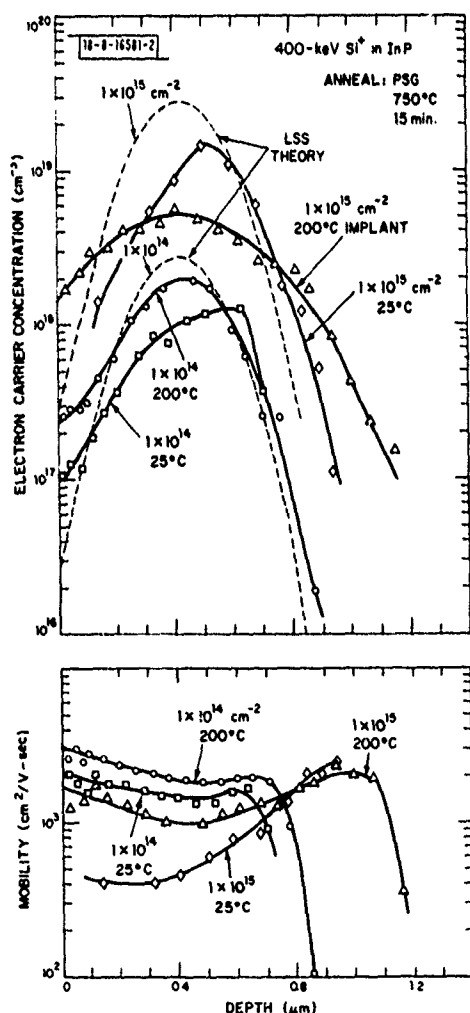
Fig. I-8. The carrier concentrations and mobilities vs depth of InP samples implanted with 400-keV Si at 25° and 200 C and with doses of 1×10^{14} and 1×10^{15} cm^{-2}. Also shown are the expected profiles calculated from the LSS range theory.

concentration and mobility vs depth for several InP samples implanted with 400-keV Si at room temperature and 200 C and doses of 1×10^{14} and 1×10^{15} cm^{-2}. Also plotted are the theoretical Si profiles for doses of 1×10^{14} and 1×10^{15} cm^{-2} which were calculated using the Johnson and Gibbons formulation of LSS theory.[22,23]

The sample implanted at room temperature with 1×10^{14} cm^{-2} had a sheet carrier concentration and mobility of 4.9×10^{13} cm^{-2} and 1600 cm^2/V-sec, respectively. This sheet carrier concentration value is on the low end of the values observed on room-temperature implanted samples [see Fig. I-1(b)], while the mobility is on the high end. This sample was chosen since it is believed that in it residual n-type damage effects are minimal and will have little effect on the measured profile. As shown in Fig. I-8, the sample has a carrier concentration near the surface which is substantially lower than expected, indicating that the implanted Si in this region is either not electrically active or compensated.

For the sample implanted at 200°C with 1×10^{14} cm^{-2} of Si, the carrier-concentration profile more nearly fits that expected from LSS theory. The measured peak carrier concentration is 2×10^{18} cm^{-2} at a depth of about 0.44 μm, which is only slightly deeper than the depth expected from LSS theory. Inclusion of higher-order moments in this range theory would probably result in even better agreement with the experimental data. The mobility for this sample implanted at 200°C is higher than that observed on the sample implanted at room temperature for all depths. The decrease in mobility in the deep tail of the profile is believed to be due to a decrease in the screening factor,[24] which results in an increase in the ionized impurity scattering from the deep levels in the Fe-doped substrate.

For the sample implanted at 200°C with 1×10^{15} cm^{-2} of Si, the peak of the measured carrier concentration is also about where it would be expected from range theory. The distribution, however, is much wider than expected indicating that substantial diffusion of the implanted Si has taken place. Samples implanted at room temperature with 1×10^{15} cm^{-2} showed a higher peak carrier concentration than the sample implanted at 200°C, but, as with the lower-dose room-temperature implant, the concentration in the region from the surface past the calculated peak is much lower than expected, again indicating that the implanted Si in this region is not electrically active or compensated. The mobility of the higher-dose room-temperature implanted sample is lower than that of the similar sample implanted at 200°C. It appears, therefore, that even for high doses, heated implants will generally be more desirable.

<div align="right">

J. P. Donnelly
G. A. Ferrante

</div>

D. GROWTH-TEMPERATURE DEPENDENCE OF LPE GaInAsP/InP LATTICE MISMATCH

Lattice matching is an important condition for GaInAsP/InP DH lasers. In the LPE growth of a GaInAsP layer on an InP substrate, the composition and lattice parameter of the epitaxial layer have been known to be functions of the growth temperature.[25,26] In this work, we report the measured growth-temperature dependence of the GaInAsP/InP lattice mismatch over a wide range of quaternary compositions.

The substrates were n-type (Sn-doped, n ~ 1×10^{17} cm^{-3}), $\langle 100 \rangle$-oriented, and polished InP wafers. A constant growth temperature was used for each LPE run. The substrate was first etched by a pure In-melt for 10 sec, then slid under the GaInAsP growth solution. The room-temperature lattice mismatch between the grown GaInAsP layer (generally 1 to 5 μm thick) and the underlying InP substrate was determined by X-ray diffraction.
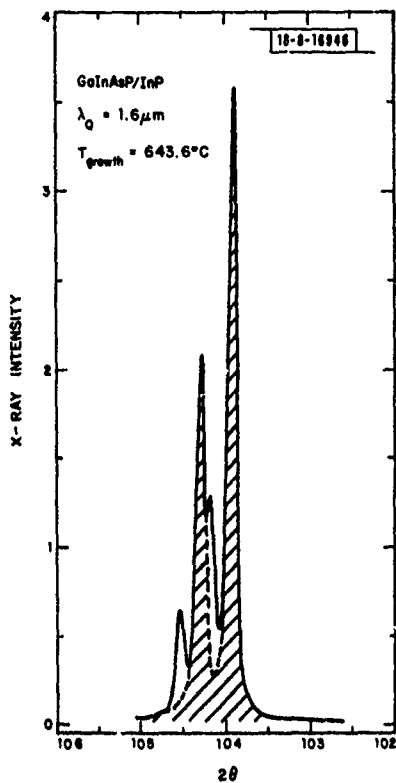
Fig. I-9. Intensity distribution of an X-ray beam after being diffracted by a GaInAsP/InP heterostructure. The two shaded peaks are the diffraction maxima due to the InP substrate and correspond to the wavelength doublet in the primary X-ray beam ($CuK_{\alpha 1}$ and $CuK_{\alpha 2}$). Overlapped with the shaded peaks are the diffraction maxima due to the GaInAsP layer (~7 μm thick). The $\Delta a/a$ corresponding to the relative shift between the two sets of maxima is -15.9×10^{-4}.

Fig. I-10. LPE GaInAsP/InP lattice mismatch as a function of growth temperature.

10
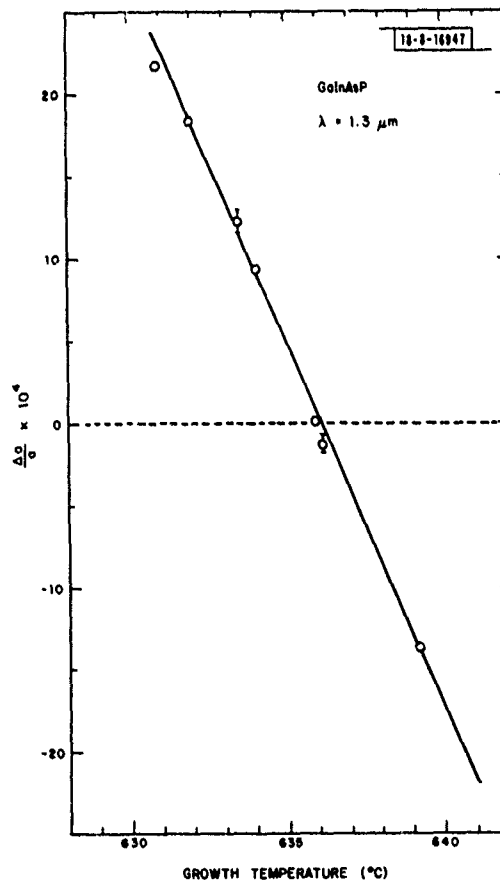
Figure I-9 shows an example of the X-ray results. The lattice mismatch, $\Delta a/a$, was obtained from the shift, $\Delta(2\Theta)$, of the diffraction maxima, based on Bragg's equation, $2a \sin\Theta = m\lambda$, with $m = 6$ and $\lambda = 1.5406$ Å. For a given GaInAsP growth solution, a different growth temperature resulted in a different $\Delta a/a$. Figure I-10 shows the growth-temperature dependence of $\Delta a/a$ obtained for a growth-solution composition which produces $\lambda_Q = 1.31$ μm at $\Delta a/a = 0$ (λ_Q is the wavelength corresponding to the energy gap of the quaternary layer). The data points in Fig. I-10 fall approximately on a straight line. One straight line of this kind was obtained for each of eight different solution compositions used in this work. In Fig. I-11 the slopes of these straight lines are plotted vs the corresponding λ_Q's.

In this work $(1/a)(\partial a/\partial T) \cong -5 \times 10^{-4}/°C$ has been observed for $1.3 \lesssim \lambda_Q \lesssim 1.55$ μm. This implies that precise temperature control to better than $2°C$ is necessary for a good lattice-matched GaInAsP/InP heterostructure. Feng et al.[26] have reported $(1/a)(\partial a/\partial T) = -2 \times 10^{-4}/°C$ for $\lambda_Q = 1.15$ μm, which is 67 percent of the corresponding value in Fig. I-11. We believe that the present value is more reliable, because our measurement was based on larger $|\Delta a/a|$'s and, therefore, had smaller errors due to signal overlap.
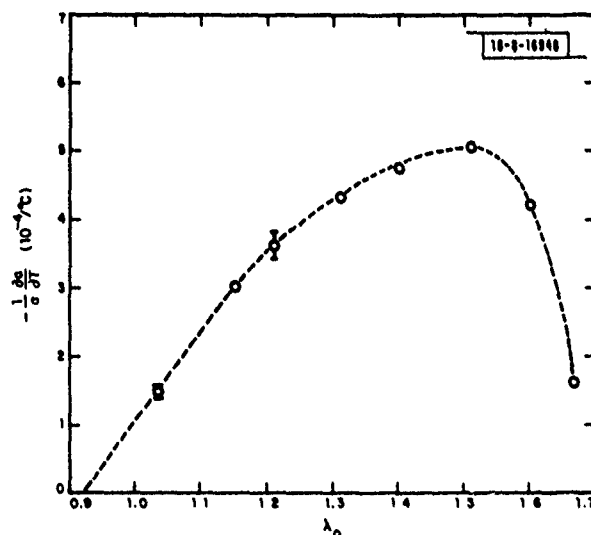
Fig. I-11. The negative of the growth-temperature derivative of the GaInAsP/InP lattice mismatch as a function of λ_Q.

Figure I-11 shows that $-(1/a)(\partial a/\partial T)$ rises almost linearly from zero for the wavelength region 0.92 μm $\leqslant \lambda_Q \leqslant 1.15$ μm. This behavior can be understood from the fact that, for those compositions, Ga and As are dilute species both in the growth solution and in the epitaxial layer. A similar argument applies to the drop of $-(1/a)(\partial a/\partial T)$ for $\lambda_g \to 1.67$ μm, where the P concentration approaches zero.

In this work, smooth GaInAsP layers have been grown directly on InP substrates without an intervening InP buffer layer. However, a buffer layer is needed for a smoother GaInAsP/InP interface in DH lasers. We have recently observed some effect of the InP buffer layer on the subsequent GaInAsP growth. Details of these experiments will be reported at a later time.

Z-L. Liau   D. E. Mull
J. J. Hsieh   J. N. Walpole
T. A. Lind

REFERENCES

1. Solid State Research Report, Lincoln Laboratory, M.I.T. (1977:4), p.1, DDC AD-A052463/7 and (1979:1), p.7, DDC AD-A073152.

2. Solid State Research Report, Lincoln Laboratory, M.I.T. (1979:4), p.9.

3. C. Armiento, private communication.

4. R. Yeats and S. H. Chiao, Appl. Phys. Lett. **34**, 581 (1979).

5. T. Miya, Y. Terumura, T. Hosaka, and T. Miyashita, Electron. Lett. **15**, 106 (1979).

6. H. Kawaguchi, K. Takahei, Y. Toyoshima, H. Nagai, and G. Iwane, Electron. Lett. **15**, 669 (1979).

7. S. Akiba, K. Sakai, Y. Matsushima, and T. Yamamoto, Electron. Lett. **15**, 606 (1979).

8. _____, 5th European Conf. on Optical Communication, Amsterdam, The Netherlands, 17-19 September 1979. Although these authors state that $\eta_d = 19$ percent/facet for the diode whose light output vs current curve is given in their Fig. 2, the value of η_d obtained from this curve is 19 percent for both facets.

9. I. P. Kaminow, R. E. Nahory, M. A. Pollack, L. W. Stulz, and J. C. DeWinter, Electron. Lett. **15**, 763 (1979).

10. J. J. Hsieh, IEEE J. Quantum Electron. **QE-15**, 694 (1979), DDC AD-A076459.

11. _____, Appl. Phys. Lett. **28**, 283 (1976), DDC AD-A025631/3.

12. J. J. Hsieh and C. C. Shen, Fiber Integ. Opt. **1**, 357 (1978).

13. J. P. Donnelly and C. E. Hurwitz, Appl. Phys. Lett. **31**, 418 (1977), DDC AD-A050856; also Solid State Research Report, Lincoln Laboratory, M.I.T. (1977:3), p.8, DDC AD-A050551/1.

14. D. E. Davies, J. P. Lorenzo, and T. G. Ryan, Solid-State Electron. **21**, 981 (1978).

15. W. T. Devlin, K. T. Ip, D. P. Leta, L. F. Eastman, G. H. Morrison, in *Gallium Arsenide and Related Compounds (St. Louis) 1978*, C. M. Wolfe, Ed. (The Institute of Physics, London, 1979), Conf. Ser. 45, p.510.

16. J. P. Donnelly and C. A. Armiento, Appl. Phys. Lett. **34**, 96 (1979), DDC AD-A069910/8; also Solid State Research Report, Lincoln Laboratory, M.I.T. (1978:4), p.1, DDC AD-A068563/6.

17. D. E. Davies, W. D. Potter, and J. P. Lorenzo, J. Electrochem. Soc. **125**, 1845 (1978).

18. D. E. Davies, J. J. Comer, J. P. Lorenzo, and T. C. Ryan, Appl. Phys. Lett. **35**, 142 (1979).

19. B. K. Shin, Appl. Phys. Lett. **29**, 438 (1976).

20. J. S. Harris, in *Ion Implantation in Semiconductors*, I. Ruge and J. Grasl, Eds. (Springer-Verlag, Berlin, 1971), p.157.

21. J. D. Sansbury and J. F. Gibbons, Radiat. Eff. **6**, 269 (1970).

22. W. J. Johnson and J. F. Gibbons, *Projected Range Statistics in Semiconductors* (Stanford University Bookstore, Stanford, California, 1970); also J. F. Gibbons, W. T. Johnson, and S. W. Mybroie, *Projected Range Statistics* (Halsted Press, New York, 1975).

23. J. Lindhard, M. Scharff, and H. Schiott, K. Dan. Vidensk. Selsk. Mat.-Fys. Medd. **33**, 1 (1963).

24. See for example: R. H. Smith, *Semiconductors* (Cambridge University Press, Cambridge, 1959), p.151.

25. J. J. Hsieh, M. C. Finn, and J. A. Rossi, Chapter 1 in *Gallium Arsenide and Related Compounds (St. Louis) 1976*, L. F. Eastman, Ed. (The Institute of Physics, London, 1977), Conf. Ser. 33b, p.37, DDC AD-A046985/8.

26. M. Feng, L. W. Cook, M. M. Tashima, T. H. Windhorn, and G. E. Stillman, Appl. Phys. Lett. **34**, 292 (1979).

II. QUANTUM ELECTRONICS

A. LIFETIME AND FLUORESCENCE FROM TRANSITION-METAL-DOPED CRYSTALS

In a previous report[1] the fluorescence properties of the laser crystals $Ni:MgF_2$, $Co:MgF_2$, and $Ni:MgO$ were described. There are other transition-metal-doped crystals which have been used in lasers and still others which are potential laser media. In this report the fluorescence lifetime as a function of temperature and the fluorescence spectra from several possibly useful laser crystals are reported.

The lifetime vs temperature curves for $^3T_2 \rightarrow {}^3A_2$ fluorescence from three different Ni-doped crystals is shown in Fig. II-1. The Ni-doping level was ~1 percent in all cases. A pulsed Nd:YALO laser operating at 1.34 μm was used as the excitation source.
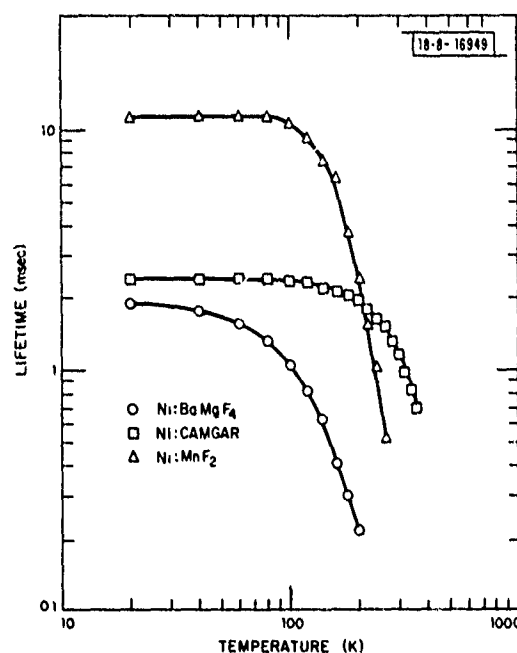
Fig. II-1. Fluorescence lifetime vs temperature for $Ni:MnF_2$, $Ni:CAMGAR$, and $Ni:BaMgF_4$.

One of the crystals examined, $Ni:MnF_2$, has been used in laser operation with both pulsed and CW lamp excitation, at crystal temperatures ranging from 20 to 85 K (Ref. 2). Laser thresholds were comparable to those observed for $Ni:MgF_2$, but untuned operation was a longer wavelength (~1.93 μm) than the 1.67-μm operating wavelength of $Ni:MgF_2$ because of the shift in fluorescence peaks between two crystals. Other notable properties of $Ni:MnF_2$ include a relatively structureless[2] fluorescence vs wavelength curve at 77 K, which could yield a smooth tuning curve compared to $Ni:MgF_2$, and the possibility of efficient transfer of excitation from Mn^{+2} to Ni^{+2}, which could produce efficient operation with broadband excitation sources. The reduction in lifetime of $Ni:MnF_2$ fluorescence at temperatures above 100 K (shown in Fig. II-1) presumed to be from multiphonon relaxation, indicates that CW laser operation will be limited to cryogenic temperatures, however. The low-temperature lifetime of 11.3 msec agrees exactly with previous measurements[2] and is characteristic of spin-allowed magnetic-dipole transitions.

13

Fig. II-2.   Fluorescence spectrum from Ni:BaMgF$_4$ at 77 K.
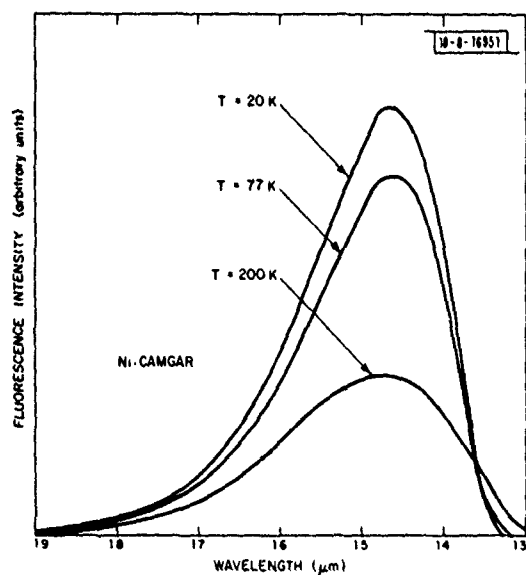
Fig. II-3.   Fluorescence spectra from Ni CAMGAR at 20, 77, and 200 K.
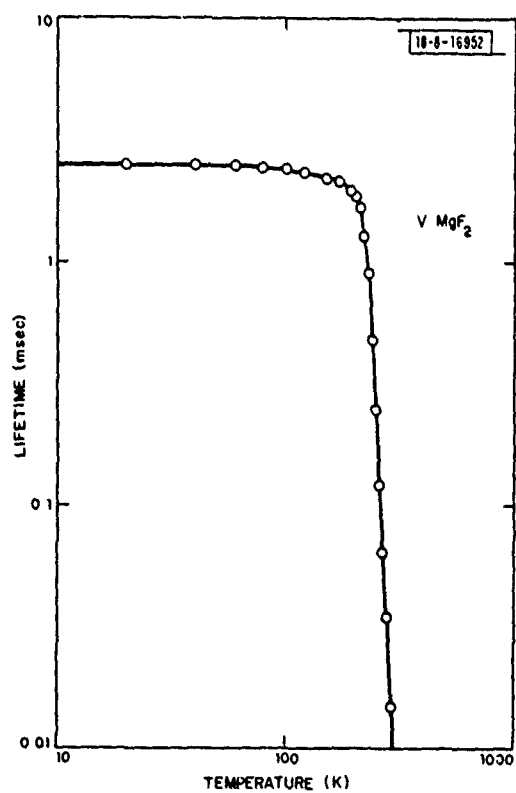
Fig. II-4.   Fluorescence lifetime vs temperature for V MgF$_2$.

BaMgF$_4$ (and similar crystals with Mg replaced by other divalent transition metals) is one of the few fluorides lacking a center of symmetry. Previous studies of this material have examined such quantities as piezoelectric constants and nonlinear optical coefficients.[3,4] The emission spectrum from a randomly oriented crystal of Ni:BaMgF$_4$ at 77 K is shown in Fig. II-2 and is somewhat similar to that observed from Ni:MnF$_2$. Zero-phonon lines do appear at lower temperatures; the 20 K emission line corresponding to the transition from the lowest-lying $^3T_2$ level to the ground state is at 1.73 μm (5780 cm^{-1}), lower in energy than in any previously reported Ni^{+2} host. From Fig. II-1, the lifetime reduction with temperature is the most severe of the crystals examined. Also, the low-temperature lifetime of 1.9 msec is considerably shorter than would be expected from Ni^{+2} in an O$_h$-symmetry environment. It is not clear whether this low value is the result of a slight admixture of odd-parity wavefunctions caused by the nature of the Ni^{+2} environment in BaMgF$_4$, or the result of residual low-temperature multiphonon relaxation as predicted by the theory of Struck and Fonger.[5] Further experiments are thus required to determine if Ni:BaMgF$_4$ has a reasonably low threshold for laser operation, even at cryogenic temperatures.

CaY$_2$Mg$_2$Ge$_3$O$_{12}$ (CAMGAR) is a cubic crystal previously used as a host for a Nd^{+3} laser.[6] The fluorescence spectra (Fig. II-3) at 20, 77, and 200 K indicate a broad, structureless emission band with no evidence of zero-phonon lines. The stronger crystal field of the oxide environment for Ni^{+2} results in relatively short-wavelength emission compared to fluoride host crystals. One notable feature of the fluorescence lifetime vs temperature curve for Ni:CAMGAR is that the 300 K lifetime is reduced by only a factor of 2 from the low-temperature value, which increases the possibility of room-temperature laser operation from this material.

Laser operation from the $^4T_2 \rightarrow {}^4A_2$ transition of divalent vanadium in MgF$_2$ (V:MgF$_2$) has been previously observed at 1.12 μm (Ref. 7). The excellent match of the broad $^4A_2 \rightarrow {}^4T_2$ and $^4A_2 \rightarrow {}^4T_1$ absorption bands to the emission spectrum of xenon flashlamps and the relatively high thermal conductivity and low nonlinear index of MgF$_2$ have recently generated interest in V:MgF$_2$ lasers for fusion drivers.[8] The fluor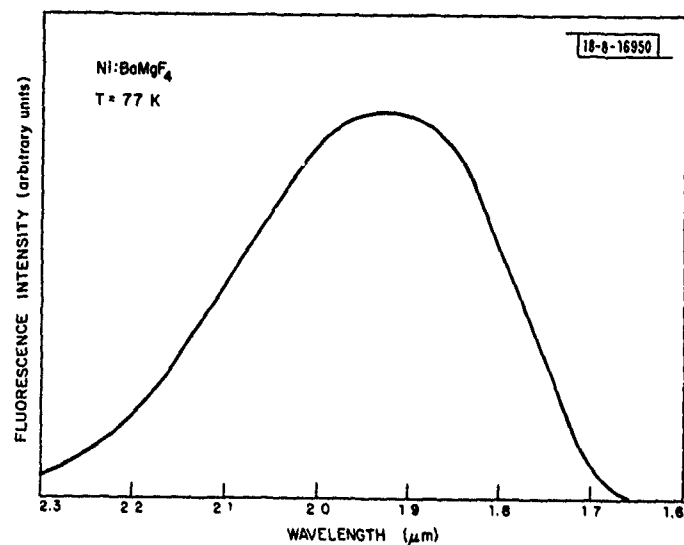escence lifetime vs temperature curve for this material is shown in Fig. II-4. Two different crystals were examined, one with a doping level of 1 wt% VF$_2$ and the other with a level at least 10 times smaller. Results were essentially the same for both crystals, and the low-temperature value of ~2.5 msec agrees well with previous data. It is apparent that low-threshold operation of V:MgF$_2$ lasers will be limited to crystal temperatures below 200 K.

P. F. Moulton

B. SCHOTTKY DIODE MIXER OPERATION AT 10 μm

We have demonstrated Schottky diode mixer operation at 30-THz carrier frequency using two laser lines in the 10-μm spectral range. By utilizing combinations of isotopic CO$_2$ laser lines, the mixers were tested with IF frequencies of 2.7, 4.8, 8.2, and 15.6 GHz. Two planar and two whisker-contacted diodes were evaluated in this study, and signal-to-noise ratios of better than 30 dB were routinely obtained at 2.7 GHz. In Fig. II-5 the 10-μm laser beats at an IF of 4 and 15 GHz are shown, where the total incident power is less than 0.5 W. At 15 GHz, second detection was accomplished by mixing the IF with a microwave synthesizer, either in the diode itself or in an external coaxial diode mixer, and then feeding the resulting RF into a 30-MHz spectrum analyzer.

4.761 GHz

LINEAR SCALE

→| |←50 kHz

15.617 GHz

LINEAR SCALE

CENTER FREQUENCY
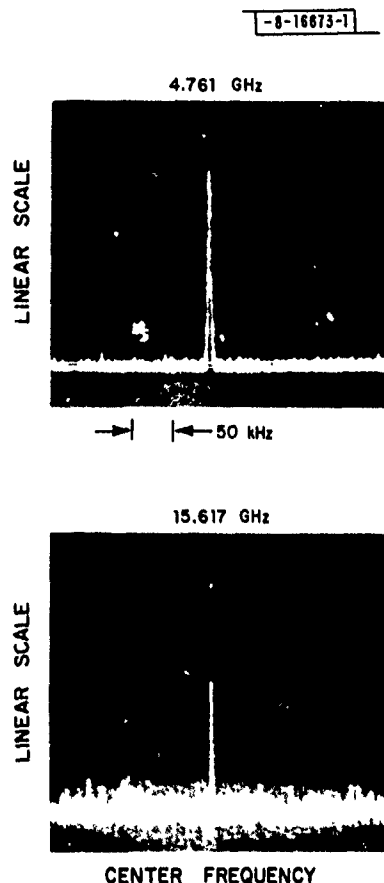
Fig. II-5. Beat note between two isotopic CO_2 lasers in GaAs Schottky diodes. Top: beat signal is displayed directly on spectrum analyzer. Bottom: beat signal is first down-converted to 30 MHz by mixing, in the diode itself, the IF with a microwave synthesizer.

Performance of GaAs Schottky diode mixers abr   the plasma frequency has been predicted[9] using an extended high-frequency model which includes skin effect, carrier inertia, and displacement currents. However, previous efforts to actually observe such mixing in Schottky diodes[10] have either failed or have been at such low IF frequencies that thermal effects could not be excluded. In the present work the 15-GHz response makes thermal effects unlikely, and we believe that tunneling (either thermionic field or simply field emission) is a dominant contributing mechanism. This would be consistent with our measurements of I-V curves of these diodes at low temperatures.

The quantum efficiency in this set of experiments is difficult to estimate since no effort has been made to couple the laser beams optimally into the diodes. Further experiments at higher IF frequencies are under way to clarify the mixing process at these wavelengths and to establish possible useful applications.

H. R. Fetterman   C. Freed
P. E. Tannenwald   R. G. O'Donnell
B. J. Clifton

16

REFERENCES

1. Solid State Research Report   Lincoln Laboratory, M.I.T. (1978:1), p. 20, DDC AD-A056715.

2. L. F. Johnson, H. J. Guggenheim, and R. A. Thomas, Phys. Rev. **149**, 179 (1966).

3. K. Recker, F. Wallrafen, and S. Haussuhl, J. Cryst. Growth **26**, 97 (1974).

4. J. G. Bergman, G. R. Crane, and H. Guggenheim, J. Appl. Phys. **46**, 4645 (1975).

5. C. W. Struck and W. H. Fonger, J. Lumin. **10**, 1 (1975).

6. E. J. Sharp, J. E. Miller, D. J. Horowitz, A. Linz, and V. Belruss, J. Appl. Phys. **45**, 4974 (1974).

7. L. F. Johnson and H. J. Guggenheim, J. Appl. Phys. **38**, 4837 (1967).

8. W. F. Krupke, private communication.

9. K. Champlin and G. Eisenstein, IEEE Trans. Microwave Theory Tech. **MTT-26**, 31 (1978).

10. M. Pyee, A. Clairon, and J. Auvray, Electron. Lett. **10**, 500 (1974).

A. EFFICIENT LARGE-GRAINED GaAs HOMOJUNCTION SOLAR CELLS

Solar cells made from both large-grained[1] and thin-film polycrystalline[2] GaAs have been limited in conversion efficiency by open-circuit voltages (V_{oc}) much less than those obtained for single-crystal GaAs cells. Although MOS structures have been employed with these materials in an attempt to improve V_{oc} (Ref. 3), values above 0.8 V have not been reported. We have now obtained conversion efficiencies exceeding 13 percent at AM1 for GaAs homojunction solar cells grown by chemical vapor deposition (CVD) on large-grained substrates. By using a new passivation method involving the surface electroplating of Sn and subsequent heat treatment, V_{oc} values approaching 0.9 V have been achieved.

The new large-grained cells utilize an $n^+/p/p^+$ structure prepared by CVD on p^+ GaAs substrates and anodically oxidized to provide an antireflection (AR) coating. Epitaxial layers were deposited in an $AsCl_3$-Ga-H_2 system under growth conditions similar to those used in the preparation of single-crystal shallow-homojunction solar cells.[4] Since variations in growth rate and surface morphology from grain to grain make measurement of growth parameters difficult, single-crystal companion substrates were used in each run. Thickness and carrier concentration measurements for the layers on the companion substrates have shown typically: $n^+ - 0.25$ μm, 3×10^{18} cm^{-3} (S); $p - 3.5$ μm, 5×10^{17} cm^{-3} (Zn); and $p^+ - 0.7$ μm, 5×10^{18} cm^{-3} (Zn). Epitaxial layer thicknesses in the large-grained samples have been found to be within a factor of 2 of the single-crystal values.

An essential step in achieving improved solar cell performance was the development of a new method for the passivation of polycrystalline GaAs. In initial experiments on small (0.2 mm^2) photolithographically defined cells using electroplated Sn top contacts and electroplated Sn or Au as a back contact, we observed that V_{oc} was markedly increased by heating the cells to temperatures in the vicinity of 200°C. For cells with Au top contacts, V_{oc} was not changed by heat treatment.

Various heating procedures were then tried on cells with Sn top contacts made from different large-grained substrates. Since numerous small cells were fabricated simultaneously by the photolithographic process, we were able to investigate cells fabricated directly on grain boundaries as well as those fabricated away from grain boundaries. Heating the cells generally caused an increase in V_{oc} and also in the short-circuit current I_{sc}, although there were variations between cells located on different parts of the same large-grained layer. Cells fabricated away from grain boundaries often showed the highest initial V_{oc}, but had insignificant improvement upon heating. For some cells V_{oc} was increased by as much as 0.5 V, and some cells had V_{oc} values above 0.9 V after heating. For some cells that were heated a number of times, each of the initial cycles caused an increase in V_{oc}, but eventually V_{oc} was degraded by additional heating.

To further understand the role of electroplated Sn in the improvement of the photovoltaic response of small cells, which appeared to be due to surface passivation of grain boundaries, we performed experiments in which Sn was electroplated on the n^+ surfaces of large-grained layers before cell fabrication. After a heating cycle, the Sn was chemically removed and the solar cell processing was continued as usual. For some layers, Sn was preferentially deposited

Fig. III-1. Large-grained GaAs homojunction solar cell (6 mm^2).

Fig. III-2. Photocurrent as a function of voltage for the cell of Fig. III-1.

AREA = 6 mm^2
J_{sc} = 21 5 mA/cm^2
V_{oc} = 0 835 V
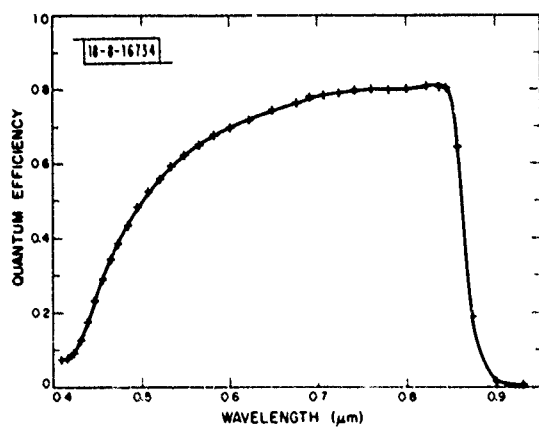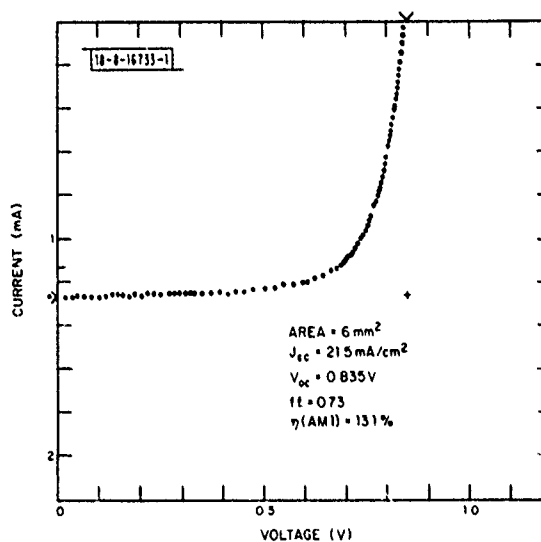ff = 073
η(AM1) = 131%

Fig. III-3. Quantum efficiency as a function of wavelength for the cell of Fig. III-1.

only on certain grain boundaries that exhibited enhanced conduction, while for other layers Sn was deposited over the entire surface. Plating of Sn over the entire surface was found to yield the most efficient larger (6.3 mm^2) cells. Of four cells fabricated on one layer that was treated in this manner, one was damaged in processing but the remaining three cells were found to have AM1 efficiencies greater than 10 percent. A micrograph of the most efficient cell is shown in Fig. III-1. More than 20 irregularly shaped grains are covered by this cell, and the varying surface morphology is evidence for different crystallographic orientations. Before the final anodization of the n$^+$ surface layer of the cell to provide an AR coating,[4] this layer was thinned by anodic oxidation and etching to remove approximately 2200 Å of GaAs. This thinning was found to increase the measured I_{sc} by 40 percent, although the increase was less rapid than would have been observed for single-crystal cells because of variations in anodic growth rate on different grains. The infrared electroluminescent emission of the three cells under forward bias was observed using a silicon vidicon. The most efficient cell showed the most intense and most uniform emission, consistent with our previous results.[5]

For the most efficient cell, the illuminated (AM1) I-V characteristic is shown in Fig. III-2, and the spectral response curve is shown in Fig. III-3. Details of the measurement techniques have been reported previously.[6] The measured parameters were V_{oc} = 0.835 V, J_{sc} = 21.5 mA/cm^2, and fill factor = 0.73, giving a conversion efficiency of 13.1 percent. The highest quantum efficiency was 0.81. The diode factor of this cell, which was measured by means of the variable illumination technique in order to eliminate series resistance effects,[7] was found to be 1.6 with a dark current of 6.9×10^{-11} A/cm^2. These values suggest that while recombination currents are not extremely high in this device, further reduction will be necessary for improved efficiency.

We speculate that the mechanism primarily responsible for the observed increase in V_{oc} is the passivation of detrimental grain boundaries by diffusion of electroplated Sn into conducting grain boundary areas. Since Sn is a donor, while we believe that grain boundaries in GaAs generally exhibit p-type conduction,* incorporation of Sn in these areas could reduce their conduction by compensation. The electroplating of Sn over the entire surface may also have the additional benefit of increasing the carrier concentration in n$^+$ surface areas that were originally more lightly doped due to variations in growth rate on the polycrystalline substrate. By this technique we have obtained the highest value of V_{oc} reported for polycrystalline GaAs solar cells of any type. The short-circuit current and the fill factor, which presently limit cell efficiency, should be increased by improving the passivation process and using a conducting top layer such as tin-doped indium oxide (ITO). We are confident that AM1 efficiencies in excess of 15 percent can be achieved.

<div style="text-align:right">

G. W. Turner   R. P. Gale
J. C. C. Fan   O. Hurtado

</div>

B. EFFICIENT SINGLE-CRYSTAL InP HOMOJUNCTION SOLAR CELLS

The theoretical conversion efficiency for InP solar cells is near that for GaAs cells.[8] However, little has been reported on InP homojunction solar cells,[9] although conversion efficiencies

---

* The evidence for p-type conduction comes from a number of experiments, including a comparison between the properties of p/n and n/p polycrystalline structures.

of 14 to 15 percent (AM2) have been obtained for CdS/InP (Ref. 10) and Sn-doped indium oxide (ITO/InP) (Ref. 11) cells. We have now fabricated InP homojunction single-crystal cells with conversion efficiencies up to 15 percent (AM1), the highest efficiency values reported for InP solar cells of any type.

The new InP cells incorporate $n^+/p/p^+$ structures obtained by growing liquid-phase epitaxial layers on (100)-oriented, $p^+(Zn \sim 10^{18}$ cm$^{-3})$ InP substrates. A $p(Zn \sim 1$ to 3×10^{17} cm$^{-3})$ layer about 2 μm thick was grown first, followed by an $n^+(Sn \sim 2$ to 5×10^{18} cm$^{-3})$ layer in the thickness range between 0.05 and 1.0 μm. Total epitaxial growth thickness was measured by edge staining and inspection with an optical microscope, while the n^+-layer thickness was determined by repeated etching of an area between two ohmic surface contacts until non-ohmic conduction was observed (indicating back-to-back diode characteristics). The cell front contact grid and active area were defined photolithographically to yield cells of 6 or 10 mm^2. Front contacts were made by electroplated Au or Sn, and back contacts were flash-evaporated Au-Mg.

The photovoltaic response of the InP cells was found to be rather insensitive to n^+-layer thickness over the wide thickness range investigated. This indicates that the surface recombination velocity is not as high for the InP cells as for our GaAs homojunction cells, whose performance is strongly dependent on n^+-layer thickness.[12] Although there was some reduction in short-circuit current for the InP cells with the thickest n^+-layers, this reduction may be due to the decreased minority-carrier diffusion length in such heavily doped regions, since appreciable optical absorption in the thick n^+-layers occurs at a significant distance from the n^+/p junction. An additional difference between our InP and GaAs homojunction solar cells is that the electron-beam-induced current (EBIC) response showed evidence of surface inversion outside the active mesa area of the InP cells, which we have not observed in our GaAs cells.

A significant problem in the development of efficient InP homojunction cells has been the preparation of an AR coating that does not degrade cell performance. Deposition of ion-beam-sputtered ITO films on the InP cells at low temperature[13] reduced the fill factor by as much as 20 percent. Investigation of these cells with a scanning electron microscope showed evidence of ITO-InP interfacial reactions, especially near the front contact fingers when electroplated Sn was used. Evidence of such reactions has been reported by others.[14] We then tried native anodic oxides grown on the InP by various techniques. Using the unmodified AGW electrolyte[15] gave nonuniformity in film thickness due to edge effects. The modified electrolyte[16] gave improved films, but their index of refraction was found ellipsometrically to be less than the optimal value (1.76) for an AR coating on InP. The best results have been obtained with an electrolyte of 0.1M monobasic ammonium phosphate,[17] using a current density of 1 mA/cm^2 at room temperature. Although the index of refraction of these films at 6328 Å is still only 1.44 ± 0.05, the thickness is uniform and the film growth can be controlled by monitoring the voltage across the electrochemical bath. The thickness was found to be linear in voltage (24 Å/V), and a thickness of 1300 Å, the optimal value for this refractive index, can easily be obtained. The use of electroplated Sn for top contact fingers permits the anodization of the cell after all other fabrication is completed.[18] This has the added benefit of separating the metallization farther from the n^+/p junction than if anodization had to be performed first.

The best InP solar cell, which was fabricated with Sn front contacts and then anodized, has an n^+-layer thickness of 0.3 μm and a p-layer thickness of 1.7 μm. The I-V characteristic of

this cell under AM1 illumination is shown in Fig. III-4. The open-circuit voltage V_{oc} is 0.779 V, the short-circuit current I_{sc} is 26.5 mA/cm^2, and the fill factor is 0.715, giving AM1, 25°C efficiency of 14.8 percent. The spectral response of this cell is shown in Fig. III-5. The details of the techniques for the efficiency and spectral response measurements have been reported previously.[6] Even though the AR coating for this cell was not optimal, over a substantial portion of the spectrum the external efficiency is approximately 0.8, indicating the good minority-carrier diffusion length in this material. The diode factor of this cell was also measured using the variable illumination technique to eliminate series resistance effects,[7] with the results shown in Fig. III-6. The low values of diode factor 1.3 and dark current 2.9×10^{-12} A/cm^2 are comparable to values obtained for GaAs homojunction solar cells grown by molecular beam epitaxy,[19] but are lower than the values for the best such cells grown by chemical vapor deposition.[20]

We feel confident that additional improvements can be made in InP homojunction solar cells. With optimized AR coatings, better material properties such as minority-carrier diffusion length, and elimination of the observed surface inversion, conversion efficiencies closer to theoretical will be obtained. The fact that efficient InP homojunction cells can be fabricated with much thicker n$^+$-layers than are possible for GaAs homojunction cells may lead to improved solar cell designs. For example, both radiation-resistant cells for space applications (where heavy damage may occur very near the surface) and cells for use in concentrated sunlight systems (where thicker n$^+$-layers would reduce the series resistance) might benefit from the utilization of InP.

<div align="right">

G. W. Turner
J. C. C. Fan
J. J. Hsieh

</div>

C. CRYSTALLIZATION FRONT VELOCITY DURING SCANNED LASER CRYSTALLIZATION OF AMORPHOUS Ge FILMS

By scanning amorphous Ge films with the slit image of a CW Nd:YAG laser to produce a solid-phase transformation to the crystalline form, we have recently prepared large-grained films containing well-aligned crystallites with dimensions up to 2 to 3×100 μm (Ref. 21). These films exhibit periodic structural features whose spatial period (d) depends on the background temperature (T_b) of the film before laser irradiation. According to a theoretical model that we have formulated for scanned laser crystallization,[22] these features are formed because the crystallization front moves in a series of rapid jumps between rest positions, with the velocity of the front (v_{ac}) during each jump much higher than the laser scanning velocity (v); their spatial period is equal to the distance between successive rest positions. Precise values of v_{ac} have not been calculated from the model because of the limited accuracy of our numerical computations. With the objective of developing scanned laser crystallization as a method for preparing low-cost Ge substrates for GaAs solar cells, we have now extended our investigation by using an optical transmission technique to measure average values of v_{ac}. The measured values range from 140 to 260 cm/sec, compared with v of only 0.5 cm/sec.

Figure III-7 is a photomicrograph showing the periodic features obtained for a Ge film 0.3 μm thick, deposited by electron-beam evaporation on a fused-silica substrate, that was laser crystallized with T_b equal to room temperature. For this film, d is about 40 μm. As reported previously,[22] each feature consists of four different regions. In Fig. III-7 the first three (a very narrow amorphous region, a small region containing a mixture of amorphous material and fine grains, and a broader region of fine crystallites) form a dark stripe whose width
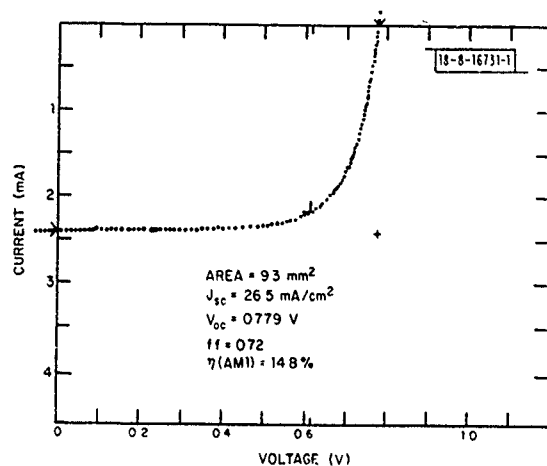
Fig. III-4. Photocurrent as a function of voltage for an InP single-crystal homojunction cell.
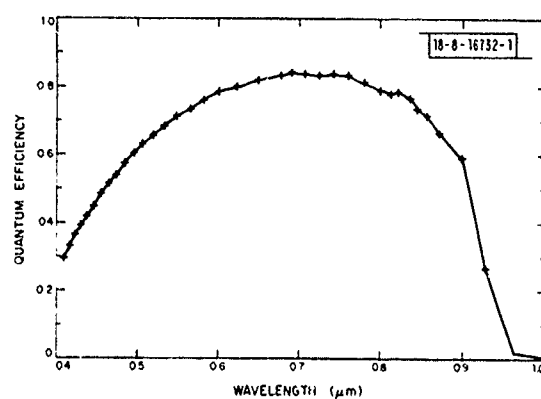

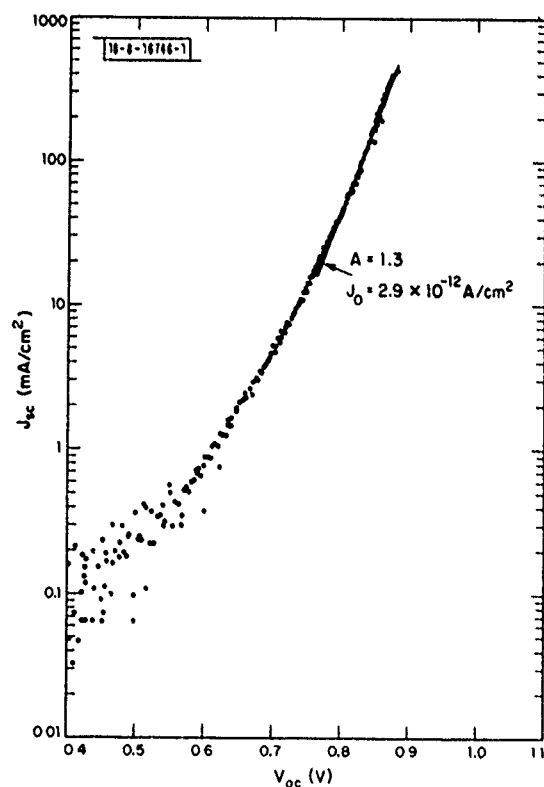Fig. III-5. Quantum efficiency as a function of wavelength for the cell of Fig. III-4.

Fig. III-6. Short-circuit current density J_{sc} as a function of open-circuit voltage V_{oc} at different illumination levels for the cell of Fig. III-4.

is about one-fifth of d, but these regions can be distinguished from each other at sufficiently high magnification. The fourth region is occupied by much larger, elongated crystallites that are generally aligned parallel to each other at an angle to the laser scan direction. When the entire crystallized area is examined, these large crystallites are seen to form a roughly chevron-like pattern, with the two halves of the pattern symmetrical about an axis that is parallel to the scan direction and located near the center of the laser slit image. Near the center of the image, the crystallites are nearly parallel to the scan direction.

To describe the periodic motion of the crystallization front (the amorphous-crystalline phase boundary) that accounts for the periodic structural features, we refer to Fig. III-8. It shows the sample geometry considered by our theoretical model and schematic laser power density profiles indicating the positions of the laser image and the phase boundary at three significant times during the crystallization process. The amorphous film is deposited on a thick substrate that is heated to T_b, and the laser image (which is assumed to have a Gaussian intensity distribution in the scanning direction) is scanned from left to right at velocity v. The approximation is made that the amorphous-to-crystalline (a-c) transformation occurs instantaneously at any point where the film temperature reaches a critical value (T_c). During crystallization the a-c boundary therefore coincides with a T_c isotherm, and the motion of the crystallization front can be found by calculating the motion of this isotherm, which is parallel to the long axis of the laser image.

The sample diagram and bottom intensity profile in Fig. III-8 show the situation at a time t_1 when the crystallization front has just come to rest, at a position close to the leading edge of the laser image, because the temperature is less than T_c for all regions of the film that have not yet been crystallized. (The shaded region under each intensity profile corresponds to the portion of the film exposed to the laser image that has remained amorphous.) After t_1, as the laser image moves forward, the temperature at the a-c boundary increases, but no further crystallization occurs until time t_2, when this temperature reaches T_c. At t_2 the laser image, having moved a distance $v(t_2 - t_1)$, is located at the position shown by the middle intensity profile, while the a-c boundary is still at the rest position it reached at t_1.

When crystallization begins at t_2, the a-c transformation is accompanied by the liberation of the latent heat of crystallization. Because the film temperature is then increased by conduction of the latent heat as well as by laser heating, the T_c isotherm and therefore the a-c boundary move forward at a velocity that is initially much higher than v. Due to the very rapid motion of the boundary relative to the laser image, the contribution of laser heating to the temperature at the boundary decreases rapidly. In spite of the continuing liberation of latent heat, at time t_3 the boundary temperature falls below T_c. The crystallization front therefore comes to rest again after having moved a distance $\bar{v}_{ac}(t_3 - t_2) = d$, the spatial period of the film structure, where $\bar{v}_{ac}$ is the front's average velocity between the two successive rest positions. At t_3, as shown by the top intensity profile in Fig. III-8, the position of the crystallization front relative to the laser image is the same as at T_1. Thus, between t_1 and t_3 both the front and the image have moved forward by the distance d. Since v is much less than $\bar{v}_{ac}$, $v(t_3 - t_2)$ is much less than d. The total distance moved by the laser image is equal to $v(t_2 - t_1) + v(t_3 - t_2)$, so that $v(t_2 - t_1) \approx d$, and $(t_3 - t_2)/(t_2 - t_1) \approx v/v_{ac}$. Thus, $(t_3 - t_2)$ is much less than $(t_2 - t_1)$. Consequently, in Fig. III-8 there is no perceptible difference between the positions shown for the laser image at t_2 and t_3.

LASER SCAN DIRECTION ——
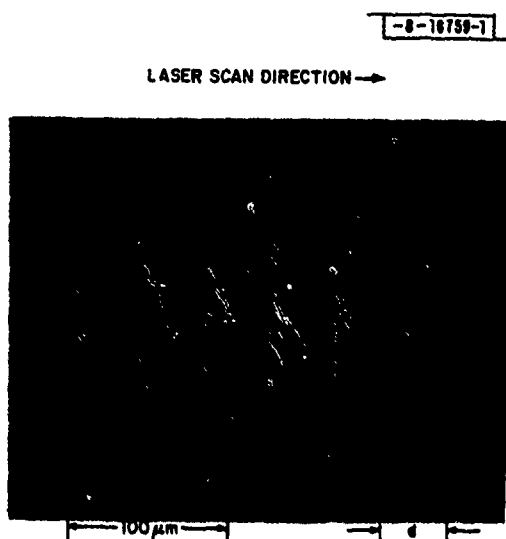

100 μm

Fig. III-7. Photomicrograph showing periodic structural features of Ge film after scanned laser crystallization.

Fig. III-8. Schematic diagram of sample geometry for scanned laser crystallization and laser power density profiles showing positions of the laser image and the amorpnous-crystalline phase boundary at three successive times during the crystallization process.
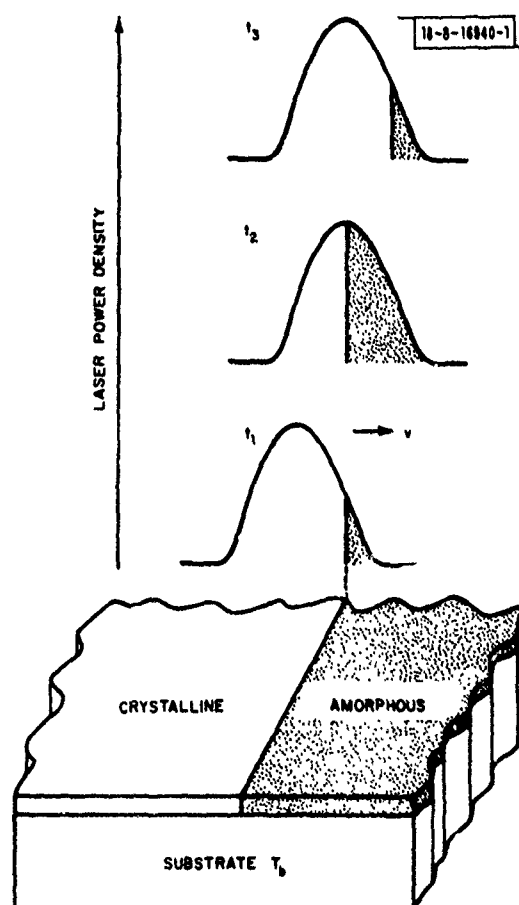
According to the preceding discussion, as illustrated by the intensity profiles of Fig. III-8, during scanned laser crystallization of a Ge film with a Nd:YAG laser the relative areas of the amorphous and crystalline regions irradiated by the laser image vary with time. Consequently, the intensity of radiation from the scanning laser that is transmitted through the film should also vary with time, since there is a marked difference in optical transmission between amorphous and crystalline Ge at 1.06 μm, the Nd:YAG emission wavelength. For Ge films 0.3 μm thick, at room temperature the transmission values for this wavelength are about 8 and 20 percent, respectively, for the amorphous and crystalline forms. Therefore the intensity of the transmitted laser radiation will have its maximum value at time t_1, when the amorphous area is smallest; the intensity will then decrease gradually to a minimum at t_2, as the amorphous area is increased by the forward motion of the laser image at velocity v while the crystallization front remains stationary; and finally the transmitted intensity will increase very rapidly, reaching its maximum value again at t_3, as the crystallization front moves forward at velocity v_{ac}. To measure v_{ac}, we have monitored the transmitted intensity as a function of time during the crystallization process.
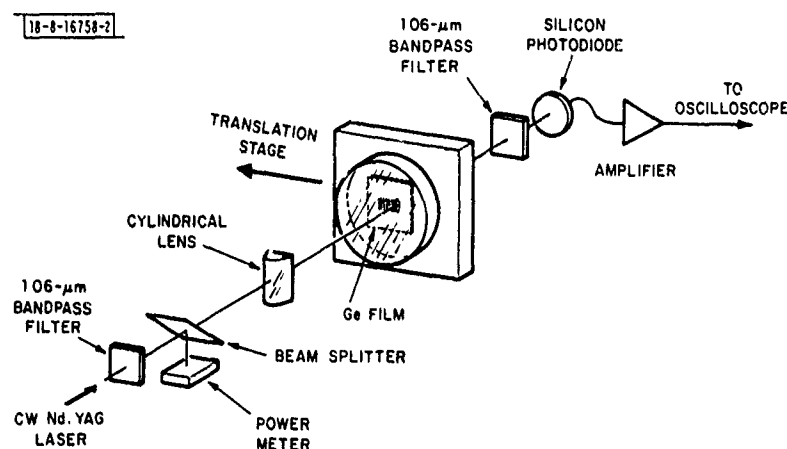
Fig. III-9. Schematic diagram of experimental system used for measuring transmitted laser radiation as a function of time during scanned laser crystallization.

The system used to measure v_{ac}, which is shown schematically in Fig. III-9, was constructed by modifying the system used in our earlier crystallization experiments[22] to permit measurement of the Nd:YAG laser radiation transmitted through the sample. The CW laser is focused to a slit image with roughly Gaussian power density distribution over a width (FWHM) of about 50 μm. The average power density, which is estimated to be about 5 kW/cm^2, was found to be uniform to ±3 percent over a length of 1.5 mm. The amorphous Ge film is mounted at the focal plane of the laser image on a transparent room-temperature platform in a flowing Ar/H$_2$ atmosphere, and the transmitted radiation is detected by a large-area Si photodiode that is attached to the platform behind the sample. A metal mask with a slit about 400 μm wide and 1 cm long is mounted between the sample and the detector so that transmission is measured only for the central region of the film where the large crystallites obtained by laser scanning are aligned approximately parallel to the scan direction. Two 1.06-μm bandpass interference filters are used to eliminate stray light. A stage driven by a synchronous motor translates the

sample platform at a constant velocity in the direction perpendicular to the long axis of the laser image, producing the relative motion of image and sample shown in Fig. III-8. The photodiode, which is operated in the photovoltaic mode, is connected through a high-speed amplifier to an oscilloscope. The diode-amplifier time constant is less than 2 μsec.

Measurements of optical transmission as a function of time were made during multiple crystallization runs on three different Ge films. As predicted by our model, the transmission varied periodically during each run, with each cycle consisting of a gradual decrease from the maximum value to the minimum value followed by a very rapid increase from minimum to maximum. Figure III-10 shows the oscilloscope traces for two successive increases in transmission
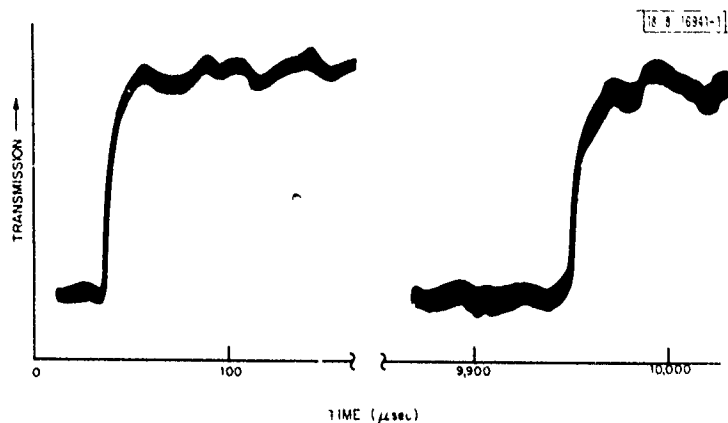
Fig. III-10. Oscilloscope traces showing photodiode signal as a function of time for two successive intervals of increasing transmission during scanned laser crystallization of Ge film.

obtained during a typical run. The time interval between these traces (corresponding to t_2 t_1 in Fig. III-8) was 9.9 msec. For the laser scan velocity of 0.48 cm/sec, this interval corresponds to d = 47 μm, in good agreement with measured spatial periods of 42 to 45 μm determined from a photomicrograph showing the periodic structural features of the crystallized film. The average velocity of the crystallization front during its motion between successive rest positions is given by $\bar{v}_{ac}$ = d/Δt, where Δt is the interval (corresponding to $t_3 - t_2$ in Fig. III-8) in which the transmission increases. For the trace on the left in Fig. III-10, Δt = 26 μsec, giving $\bar{v}_{ac}$ 180 cm/sec. This trace shows that the rate at which the transmission increases is initially constant but decreases as the transmission approaches its maximum value. This variation, which was observed in all the experiments, can be attributed primarily to the variation in power density across the width of the laser image.

Twelve pairs of d and $\bar{v}_{ac}$ values, each obtained by measuring two successive oscilloscope traces like those in Fig. III-10, have been determined. The values of d range from 36 to 46 μm, and the values of $\bar{v}_{ac}$ range from 140 to 260 cm/sec. There is no systematic difference between the results for the three different Ge films. We conclude that the optical transmission experiments confirm our theoretical model of scanned laser crystallization, which attributes the periodic structural features of the films to the intermittent motion of the crystallization front at velocities much higher than the laser scanning velocity.

R. L. Chapman   H. J. Zeiger
J. C. C. Fan   R. P. Gale

REFERENCES

1. Y. C. M. Yeh, F. P. Ernest, and R. J. Stirn, in 13th IEEE Photovoltaic Specialists Conference – 1978 (IEEE, New York, 1978), p. 966.

2. S. S. Chu, T. L. Chu, and M. S. Lan, J. Appl. Phys. 50, 5805 (1979).

3. Y. C. M. Yeh and R. J. Stirn, Appl. Phys. Lett. 33, 401 (1978).

4. J. C. C. Fan, C. O. Bozler, and R. L. Chapman, Appl. Phys. Lett. 32, 390 (1978), DDC AD-A058281/7.

5. G. W. Turner, J. C. C. Fan, and J. P. Salerno, Solar Energy Research Institute Report No. TP-49-185, p. 107 (1979).

6. C. O. Bozler and J. C. C. Fan, Appl. Phys. Lett. 31, 629 (1977), DDC AD-A053926/2.

7. J. C. C. Fan, R. L. Chapman, J. P. Donnelly, G. W. Turner, and C. O. Bozler, Appl. Phys. Lett. 34, 780 (1979), DDC AD-A073884.

8. J. J. Wysocki and P. Rappaport, J. Appl. Phys. 31, 571 (1960).

9. Early work: P. Rappaport, RCA Rev. 20, 373 (1959); many authors refer to J. L. Shay, K. J. Bachmann, and E. Buehler, Appl. Phys. Lett. 24, 192 (1974), which gives results for InP p-n junctions but not for solar cells.

10. J. L. Shay, S. Wagner, M. Bettini, K. J. Bachmann, and E. Buehler, IEEE Trans. Electron Devices ED-24, 483 (1977).

11. K. S. SreeHarsha, K. J. Bachmann, P. H. Schmidt, E. G. Spencer, and F. A. Thiel, Appl. Phys. Lett. 30, 645 (1977).

12. J. C. C. Fan, C. O. Bozler, and B. J. Palm, Appl. Phys. Lett. 35, 875 (1979).

13. J. C. C. Fan, Appl. Phys. Lett. 34, 515 (1979), DDC AD-A072667/9.

14. K. J. Bachmann, H. Schreiber, Jr., W. R. Sinclair, P. H. Schmidt, F. A. Thiel, E. G. Spencer, G. Pasteur, W. L. Feldman, and K. S. SreeHarsha, J. Appl. Phys. 50, 3441 (1979).

15. A. Colquhoun and H. L. Hartnagel, Surf. Technol. 5, 291 (1977).

16. B. Bayraktaroglu et al., Final Technical Report, DAERO-76-G-019, Dept. of the Army European Research Office (January 1977), p. 23.

17. D. Law and C. A. Lee, J. Electrochem. Soc. 123, 768 (1976) – results for dibasic solution; we have found monobasic to give similar results.

18. C. O. Bozler, J. C. C. Fan, and R. W. McClelland, Chapter 5 in Gallium Arsenide and Related Compounds (St. Louis), 1978 (The Institute of Physics, London, 1979), p. 429, DDC AD-A072370.

19. J. C. C. Fan, A. R. Calawa, R. L. Chapman, and G. W. Turner, Appl. Phys. Lett. 35, 804 (1979).

20. J. C. C. Fan and C. O. Bozler, in 13th IEEE Photovoltaic Specialists Conference – 1978 (IEEE, New York, 1978), p. 953.

21. J. C. C. Fan, H. J. Zeiger, R. P. Gale, and R. L. Chapman, Appl. Phys. Lett. 36, 158 (1980); Solid State Research Report, Lincoln Laboratory, M.I.T. (1979:4), pp. 43-47.

22. H. J. Zeiger, J. C. C. Fan, B. J. Palm, R. P. Gale, and R. L. Chapman, Proc. Symp. on Laser and Electron Beam Processing of Materials, Materials Research Society, 1979 Annual Meeting (to be published); Solid State Research Report, Lincoln Laboratory, M.I.T. (1979:2), pp. 41-45, DDC AD-A078676.

IV. MICROELECTRONICS

A. GRAPHOEPITAXY OF SILICON ON FUSED SILICA USING SURFACE MICROPATTERNS AND LASER CRYSTALLIZATION

Since publication of our initial results on the graphoepitaxy of silicon on fused-silica substrates,[1,2] we have set up an x-ray pole plotting apparatus which permits a quantitative evaluation of orientation and texture. Measurements of the width of the (400) diffraction peak as a function of angle relative to the substrate normal and the widths of the four (220) peaks as a function of rotation about the substrate normal indicated that there was a distribution of orientation in the graphoepitaxial silicon prepared by CW argon laser crystallization as described earlier.[1] On 3.8-μm spatial-period surface gratings, the [100] directions are parallel to the grating to within ±15° and perpendicular to the substrate surface to within ±1.5. Decreasing the grating spatial-period, increasing the grating depth, improving the cross-sectional profile and line edge smoothness, increasing the substrate temperature during crystallization, and increasing the number of raster scans all serve to decrease the spread in orientations.

Laser crystallized films were analyzed in a transmission electron microscope (TEM). Distinct grains were clearly discernible in the silicon from outside the grating area, but no grain boundaries were visible in the silicon from inside the grating area, although the x-ray results indicate the presence of distinct grains. No slip planes, dislocation loops or twins were observed by TEM. Figure IV-1 shows a transmission diffraction pattern taken in the TEM of the silicon over the grating. The Kikuchi lines in the diffraction pattern indicate a highly ordered crystalline structure.
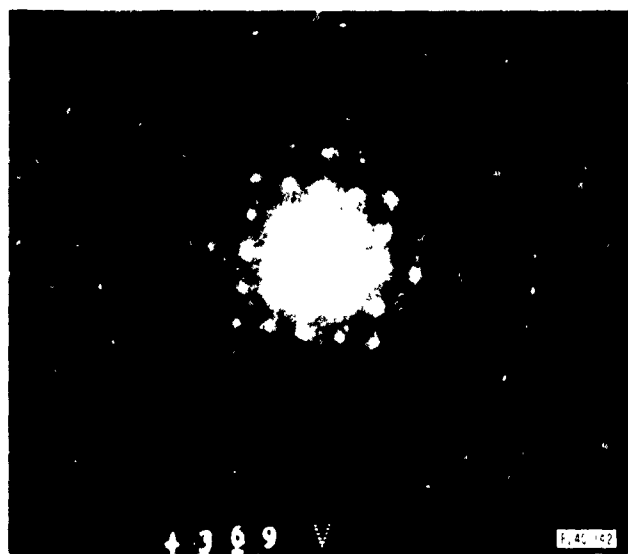

Fig. IV-1. Transmission electron diffraction pattern of a 500-nm-thick silicon film laser crystallized over a 3.8-μm-period square-wave grating in amorphous fused silica. The electron beam was perpendicular to the silicon film yielding a (100) diffraction pattern. The Kikuchi lines visible in the pattern indicate a high degree of crystalline perfection.

The graphoepitaxial silicon films have an irregular surface roughness with amplitude of several 10 nm and minimum period typically $\gtrsim$ 50 μm. In addition, there are intersecting microcracks, with separation ranging from tens of micrometers to ~1 mm. These microcracks tend to lie along major crystallographic directions, particularly $\langle 110 \rangle$. We believe these cracks are due to stresses induced by laser crystallization. Fewer microcracks form if the substrate is heated to a few hundred degrees centigrade during laser crystallization.

Because of surface roughness and microcracks, we did not attempt to fabricate devices or make Hall mobility measurements on this material. We have, however, measured sheet resistivity. Amorphous silicon films 0.5 μm thick on top of surface gratings were doped by ion implantation with boron or phosphorus prior to laser crystallization using four different ion energies in order to achieve a nearly uniform doping of 2.4×10^{17} atoms/cm^3 throughout the silicon film. Subsequent laser crystallization both activated the dopant and induced uniform orientation. Bulk silicon wafers were also implanted in the same manner to serve as controls. The phosphorus was implanted at 35-Ω-cm p-type wafers and the boron was implanted at 30-Ω-cm n-type wafers. These silicon wafers were then annealed at 900°C for 30 min. Four in-line Cr/Au dots, 1.4 mm in diameter spaced 1.5 mm apart, were fabricated on the surfaces of both the graphoepitaxial silicon and the control wafers enabling four-point-probe measurements to be made. The samples of graphoepitaxial silicon showed a large variation in sheet resistance depending upon the substrate temperature during laser crystallization. The best results were obtained on phosphorus-implanted samples which were mounted on a heating stage held at 540°C during laser crystallization. The sheet resistance was a factor of 2.5 times larger than that of the phosphorus-doped silicon wafer used as a control, and the mobility of electrons in the graphoepitaxial silicon can be inferred to be 40 percent of bulk mobility or better since surface roughness and microcracks in the 0.5-μm-thick silicon almost certainly produce scattering and reduce the apparent mobility.

M. W. Geis   D. Antoniadis
D. C. Flanders   H. I. Smith
D. J. Silversmith

B. CHARGE-COUPLED DEVICES: SAW ACCUMULATING CORRELATOR WITH CCD READOUT

An earlier report[3] described an accumulating correlator in which the multiplication and time-integration of many samples of two wideband surface-acoustic-wave (SAW) inputs take place in a charge-coupled device (CCD). This report describes the physical mechanisms by which the accumulation process takes place.

A schematic diagram of the correlator is shown in Fig. IV-2. The CCD is coupled to a piezoelectric delay line across a gap by means of an array of conductive sampling fingers. The SAW inputs counterpropagate on the delay line, and the cross-correlation of the two SAWs is subsequently read out from the CCD. Electric fields accompanying the signal and reference SAWs are sampled by the fingers and mixed by nonlinearities in the silicon substrate, and the DC component of the mixing products is accumulated in the CCD. The charge in each CCD well, therefore, represents a discrete sample of the correlation between signal and reference.

This accumulation process takes place in an RC integrator formed by the transfer gates and the CCD φ_1 gates, with the nearly pinched-off transfer channel forming the resistor and the φ_1 well forming the accumulation capacitor. Mixing action occurs in the varactor-like nonlinearity of the drain region of the bias transistors, and the product of reference and signal SAWs accumulates in the RC integrator to produce the desired correlation between signal and reference.
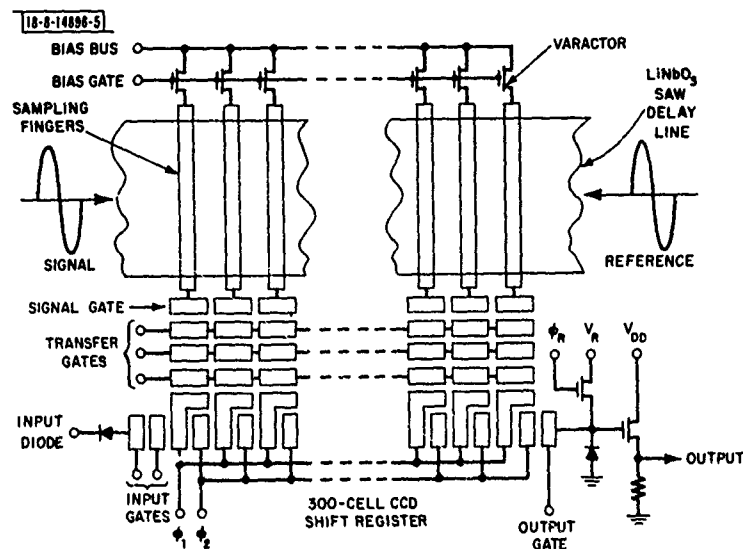
Fig. IV-2. Schematic diagram of the SAW/CCD accumulating correlator.

The accumulation process is strongly dependent on the bias voltage applied to the gate control-ling the nearly pinched-off integrating channel. As a result, this gate must be biased by a stable DC voltage source to set and maintain the RC time constant, and appropriate clock waveforms applied to an intermediate transfer gate must be used to properly sequence the device.

Operation of the accumulating correlator with a stable potential on the integrating channel has enabled us to increase the linear accumulation time to 10 msec, but with low dynamic range. The dynamic range is limited by fixed-pattern noise, much of which is signal independent and can be compensated by adequate processing of the CCD output. One possibility is to store and delay the fixed-pattern noise in a CCD analog delay line and subsequently subtract it from the output signal. We are also studying the causes of the fixed-pattern noise and exploring ways to minimize it in order to realize the full signal-processing advantage provided by the 2×10^5 time-bandwidth-product waveform. A self-correlation effect (important in the presence of CW jam-mers) also exists which is caused by multiple internal reflections within the SAW delay line, a problem that can be minimized by appropriate redesign of the SAW delay line.

D. L. Smythe
R. W. Ralston

C. CHARGE-COUPLED DEVICES: MULTIPLYING D/A CONVERTER

A multiplying, digital-to-analog converter (MDAC) of novel design, which uses capacitance-weighted CCD inputs, has been implemented using buried-channel CCD techniques. The device is capable of high-speed, low-power operation, and can be integrated on-chip with signal-processing CCDs such as transversal filters. This latter feature is important for CCD filters such as the chirp-z transform[4] or systems where the CCD must process digitized signals.

A photomicrograph of the MDAC chip is shown in Fig. IV-3. Each chip incorporates two complete devices, identical except that the two input gates (labeled ϕ_1 and V_{in} in Fig. IV-4) are surface channel in device "S" and buried channel in device "B". The devices with surface-channel inputs are part of a program to evaluate the possibility of reducing fixed-pattern noise
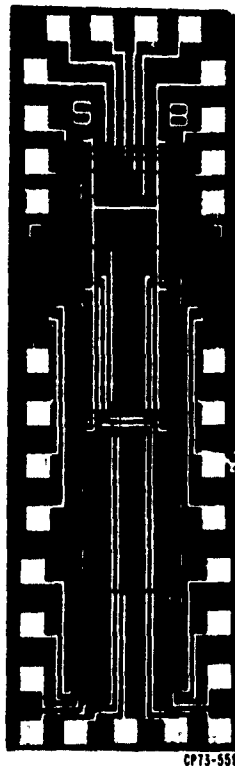
Fig. IV-3. Photomicrograph of the MDAC chip. Each chip incorporates two complete 8-bit D/A converters; the devices are identical except that the one labeled "S" uses surface-channel input gates, and the one labeled "B" uses buried-channel input gates.
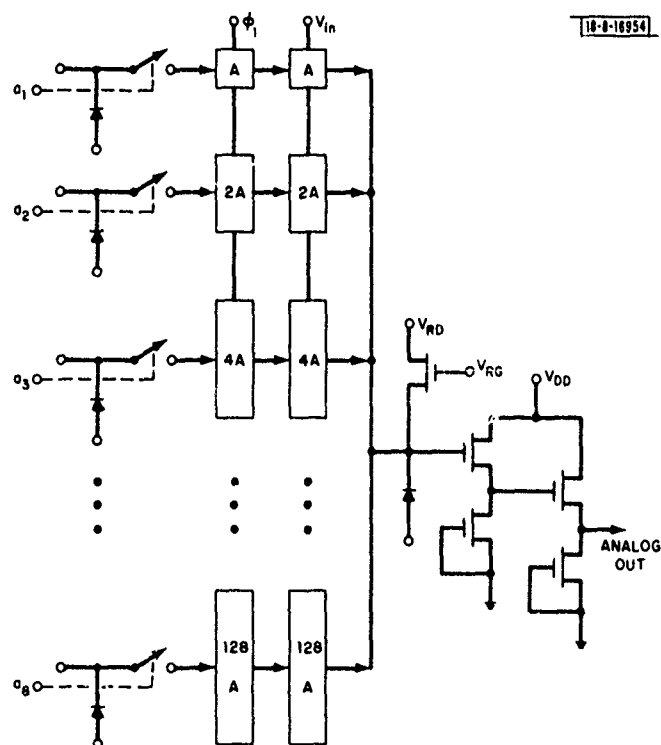

Fig. IV-4. Schematic of the MDAC.

in buried-channel CCDs by using surface-channel inputs.[5] Each MDAC consists of eight paral-lel CCD channels with binary-weighted input-gate capacitances for D/A conversion of 8-bit words. An input technique similar to the one for our previously reported programmable transversal filter was used.[6] A schematic of the device is shown in Fig. IV-4. The input diode level of each channel is controlled by the corresponding bit of a digital word. When the digital input is a "0", the diode is at a low level and a charge packet can be transferred to the CCD's summing node. The amount of charge transferred in the ith channel, Q_i, is determined by V_{in}, the analog mul-tiplying signal applied on the signal gate, according to the following equation:

$$Q_i = \frac{128}{2^{i-1}} C_{min} a_i (V_{in} - \varphi) \qquad i = 1, 2, \ldots, 8$$

where C_{min} is the input gate capacitance of the least significant bit, a_i is the ith bit of a digital word, and φ is a fixed reference voltage. When the digital input is a "1" and the input diode is at a high level, no charge can be transferred. The output of the eight parallel channels are sum-med in the charge domain, and the analog output is detected by floating diffusion output circuitry and an on-chip, two-stage source follower. Since the device will accept digital inputs directly from a TTL source when the substrate is biased, no TTL-to-MOS buffer is needed.

The MDAC was tested by digitizing an 8-kHz sine wave to 8-bit accuracy and applying the resulting digital signal to the device's input diodes at a 10-MHz digital-word data rate. The multiplying signal, V_{in}, for this test was a 1.4-kHz sine wave. The multiplying signal and the analog output signal from the MDAC are shown in Fig. IV-5 and demonstrate the excellent lin-earity of the device.
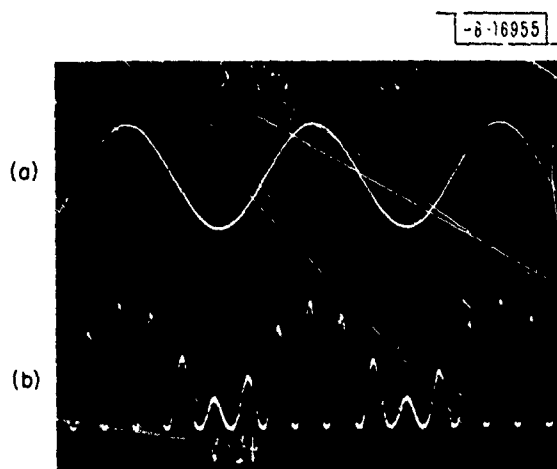
A. M. Chiang
B. E. Burke

Fig. IV-5. (a) 1.4-kHz sine-wave multiplying input signal. (b) Output from the MDAC when an 8-kHz wave is digitized to 8-bit accuracy and the resulting digital signal is applied to the inputs of the MDAC and multiplied by the 1.4-kHz sine wave of (a).

D. CHARGE-COUPLED DEVICES: GALLIUM ARSENIDE CCDs

Because GaAs has a higher electron-carrier velocity than silicon to fields of 2×10^3 V/cm (Ref. 7), GaAs integrated circuits are expected to operate at considerably higher frequencies. A theoretical analysis and an experimental characterization of GaAs CCDs are being performed to understand and capitalize on the expected high-speed performance of these devices. We describe here the results of our initial experiments, with special emphasis given to the design, fabrication, and testing of the first 2-phase GaAs CCD to be reported.

Fabrication techniques have been developed for both 3- and 2-phase GaAs CCDs. A 3-phase GaAs CCD is shown in Fig. IV-6. The Schottky barrier gates for input, output, and charge transfer as well as input and output ohmic contacts are contained in the 3-phase CCD. A crossover technology using plasma-deposited Si_3N_4 is necessary in order that all three phases be accessible through peripheral bonding pads. A cutaway representation of the 3-phase CCD is shown in Fig. IV-7 with the Si_3N_4 passivation omitted. The devices were fabricated in an n-epilayer
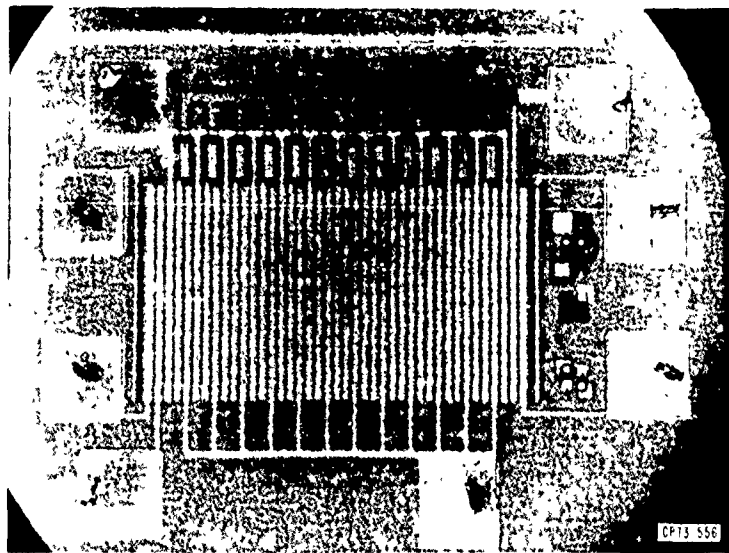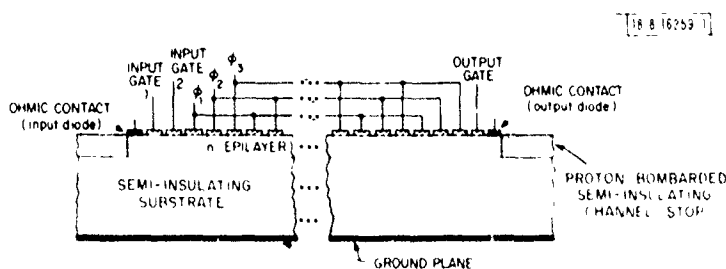

Fig. IV-6.   A 3-phase GaAs CCD.

Fig. IV-7.   Cutaway representation of a 3-phase CCD.

on a Cr-doped semi-insulating substrate. This structure provides buried-channel operation with charge residing in the epilayer near the epilayer/substrate interface. The semi-insulating substrate provides a low stray capacitance with the resulting fast clocking capability.

The Schottky barriers were formed by evaporating Ti-Au and etching 2-μm gaps using standard photolithography. Ohmic contacts were made by evaporating and alloying Ni-Ge-Au. A 250-keV proton bombardment with a fluence of 10^{14} cm^{-2} converted the GaAs surrounding the active CCD to semi-insulating material to provide charge confinement. The back side of the wafer has a Ti-Au ground plane to provide control of the potentials in the depleted regions of the epilayer.

The potentials necessary for charge transfer in the 3-phase CCD are produced by clock voltages applied to each phase. Charge is injected with the fill-and-spill technique, whereby the input diode is pulsed to allow electrons to pass over the barrier formed below the first input gate and to fill the well below the second input gate. This charge packet is then transferred when phase one of the CCD rises to its highest potential. Two off-chip GaAs MESFETs are used in the output stage, where one FET acts as a reset device and the other as a follower. This 3-phase device was tested at 100 kHz and had a charge-transfer efficiency of 0.99.

In order to overcome many of the problems inherent in 3-phase GaAs CCDs, a 2-phase CCD technology was developed. A picture of a 2-phase, 33-transfer-gate device is shown in Fig. IV-8.
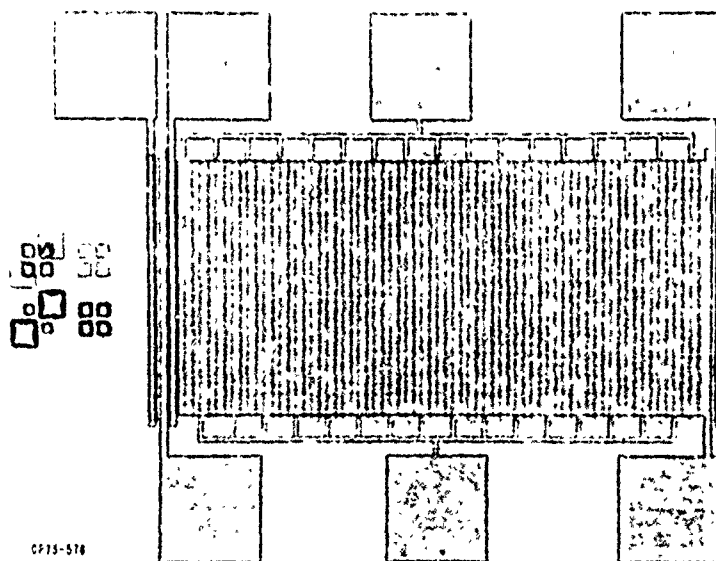
Fig. IV-8. A 2-phase GaAs CCD.

The same material, Schottky barrier input, output, and transfer-gate structure and proton-bombarded channel-stops are used as in the 3-phase CCD. However, three distinct differences in the 2-phase device provide several advantages over the 3-phase version. First, the need for a crossover technology has been eliminated. Second, the problems associated with producing submicrometer gaps between electrodes by photolithography have been eliminated. Third, a 2-phase device makes clocking the CCD simpler as discussed below.

The key to the 2-phase operation of this device are the etched steps (Fig. IV-9) in the GaAs which form potential barriers in the bulk. These steps provide unidirectional charge flow during 2-phase operation. Instead of using three different clock voltages as in the 3-phase structure, two barriers in each cell are produced by the difference in epilayer thickness below the transfer gates. Figure IV-10 shows the one-dimensional electron potential for an empty well of a CCD

Fig. IV-9. Cutaway representation of a 2-phase CCD.

Fig. IV-10. One-dimensional empty well electron potential for two different epilayer thicknesses: (a) thicker epilayer and (b) thinner epilayer.

38

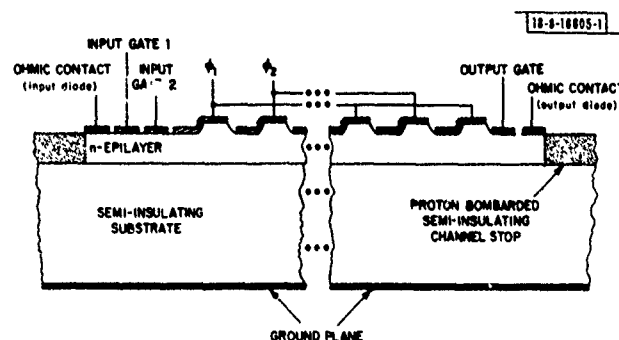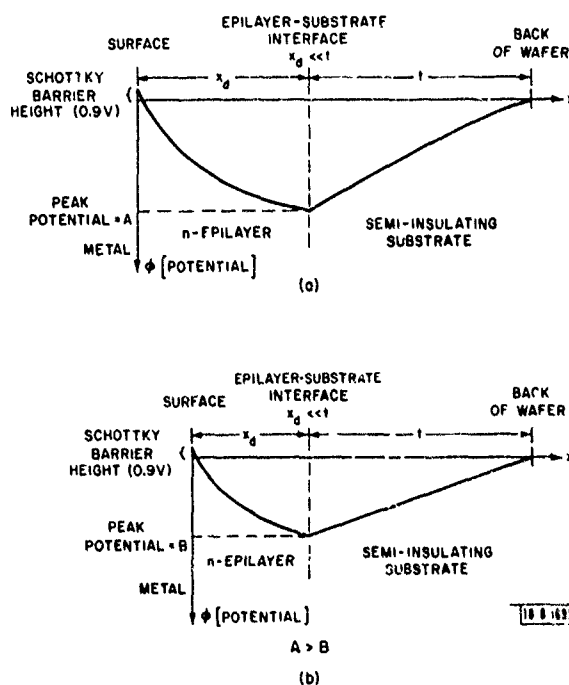for two different epilayer thicknesses. It is assumed in Fig. IV-10 that zero volts is applied to the Schottky barrier, that the epilayer is depleted of charge, and that the back of the wafer is grounded. Because the epilayer thickness, x_d, is much less than the substrate thickness, t, there is a scale change in Fig. IV-10 at the interface in order to show the epilayer potentials more clearly. The peak potential is higher for the thicker epilayer than the thinner epilayer. This difference in peak potentials produces the lateral electric fields necessary to transfer charge and provides the barrier to charge flowing backward.

These potential steps allow the clocking of the CCD with 2-phases. By applying different voltages to phase 1 and phase 2, four potential levels are produced inside each cell of the CCD. Two different clocking schemes can be used to transfer charge. One scheme is 2-phase clocking, where both phase 1 and phase 2 have oscillating voltages. The position of the deepest well, and thus the charge packet, moves from the area below phase 1 to below phase 2, and then again below phase 1 transferring charge in one direction. Alternately, one phase can be held at a constant voltage with the other phase oscillating above and below that level (uniphase clocking). This method simplifies clocking by requiring one less input signal, but can only handle one half the charge packet for an equivalent clock voltage swing. Sine-wave clocking, which is expected for 1-GHz clock waveforms, can be used in both cases.

The technique for forming submicrometer gaps between electrodes without photolithography can be understood from the cutaway representation of the 2-phase device in Fig. IV-9. Each transfer electrode covers both a thin and thick region of the epilayer. Evaporation at a 45° angle provides continuity on one side of the raised GaAs and a shadowed gap on the other side. The GaAs epilayer thickness difference of 0.5 μm (produced by chemical etching) causes a gap of approximately 0.5 μm for these evaporation conditions.

The performance of a 2-phase CCD operated with uniphase clocking is shown in Fig. IV-11. Thirty pulses are injected into the CCD (shown on the lower portion of Fig. IV-11) and are
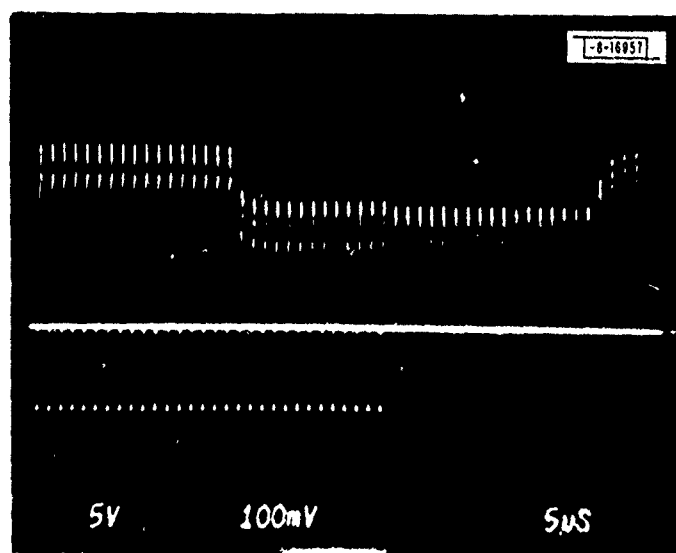
Fig. IV-11. Results obtained from a 2-phase CCD using uniphase clocking. Thirty input pulses are shown on the lower trace, with the corresponding output in the top trace. The pulses are delayed by 16.5 clock cycles due to the 33 transfer gates of the CCD.
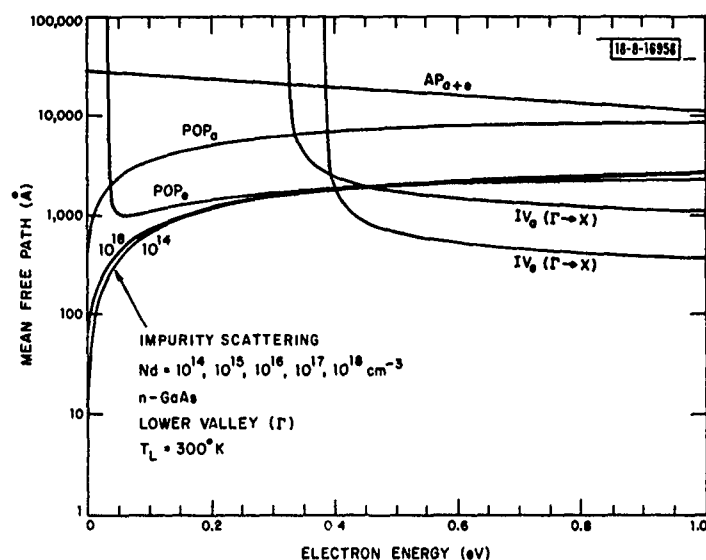
Fig. IV-12. The mean-free paths of scattering events in the lower valley for GaAs. (POP, polar optical phonons; AP, acoustic phonons; IV, intervalley transfer; subscripts a and e denote absorption and emission, respectively).
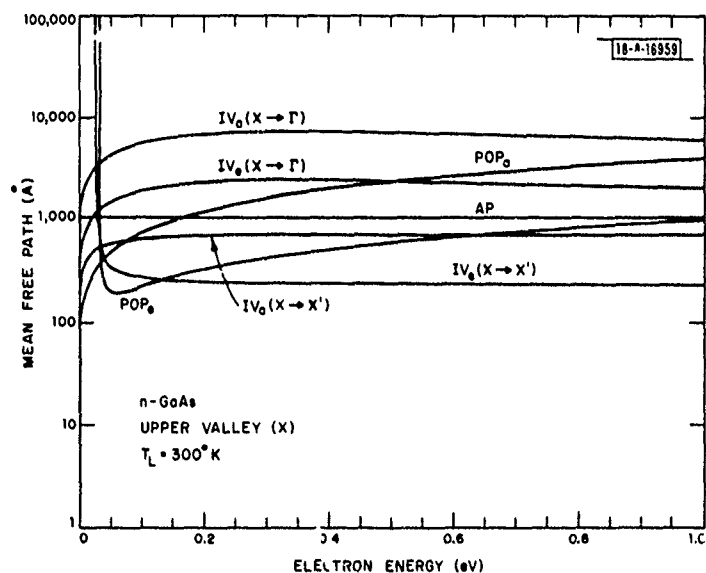
Fig. IV-13. The mean-free paths of scattering events in the upper valley for GaAs.

delayed by 16.5 clock cycles because of the 33 transfer gates of the 2-phase CCD. The output pulses are the upper trace of Fig. IV-11. The transfer efficiency is 0.993 from 1 to 10 MHz. The test setup and the off-chip detection stage did not permit measurement above 10 MHz. The transfer inefficiency is attributed to traps in the active epilayer, traps in the semi-insulating substrate near the epilayer interface, and leakage current in the Schottky barriers. Using deep-level transient spectroscopy, a study of the trapping mechanisms will be performed to model the transfer characteristics more accurately. Eliminating trapping centers requires both higher quality substrate material and techniques to grow higher quality epilayers free of high concentrations of deep traps.

Another generation of devices is being designed to extend the frequency of the 2-phase CCDs closer to 1 GHz. The cell area of these devices will be 25 percent of the present cell size with a length and width of 20 and 100 μm, respectively. The gate capacitance should be reduced by a factor of 4, thereby reducing the power requirements of the clock driver circuitry as well as increasing the clock frequency. One difficulty with the present structure is the large step height in the GaAs which produces a well voltage (potential difference under each electrode) of approximately 5 V. Thus for uniphase operation the clock voltage must swing through at least 10 V, which is difficult to achieve at frequencies near 1 GHz because of the large capacitance of the Schottky barrier gates. Therefore, the next generation CCD is being designed with slightly lower epilayer doping and thickness to produce well voltages closer to 2 V. This will mean smaller charge packets, but by including the output circuitry on-chip the output node capacitance will be significantly reduced, and a reasonable output signal should be achieved at gigahertz clock rates.

<div align="right">G. L. Hansell</div>

E. HIGH-FREQUENCY CONSIDERATIONS IN SEMICONDUCTOR DEVICES

The physical principles which are used in modeling electronic devices must be continually scrutinized as the size of the device decreases or the frequency of operation increases. This is especially true for high-mobility materials such as GaAs and InP, which are commonly used for millimeter-wave applications, where the basic transport mechanisms are altered for sub-micrometer devices and for frequencies above 10 GHz.

The underlying physical events which govern transport properties are electron-phonon interactions, impurity scattering, alloy scattering, intervalley scattering, and contact phenomena. The basic scattering mechanisms in bulk semiconductors have been studied for the past decade[8-10] but with the exception of the Gunn device there has been little consideration given to these mechanisms in device design. What is particularly useful for the device designer is a comparison of the mean free paths which result from considering each scattering mechanism individually. Figure IV-12 shows the important scattering events for n-type GaAs, where the mean free path is shown as a function of electron energy in the lower (Γ) valley. The mean free paths were calculated from expressions for the collision frequencies used in Monte Carlo simulations of bulk semiconductors.[8-10] The polar optical phonon is the dominant intravalley scattering mechanism in lightly doped GaAs for small electron energies. At higher energies nonequivalent intervalley ($\Gamma \rightarrow X$) transfer to the upper valley dominates. The mean free path for impurity scattering is not greatly affected by the doping density. The mean free paths for the upper (X) valley are shown in Fig. IV-13. The polar optical phonons again dominate at small energies. At higher energies the equivalent intervalley ($X \rightarrow X'$) scattering is the dominant process. Current

experimental evidence indicates that the lowest upper valley may be of L symmetry with the X valley just slightly higher in energy. This does not significantly alter the transport properties of GaAs or the general picture shown in Fig. IV-13.

The mean free path only gives a partial picture of the scattering process since some of the collision events are not isotropic. Polar optical phonons and impurity scattering are both predominately small angle scattering events and hence less effective in changing the electron momentum. In order to calculate the mobility of a material both the mean free path and the scattering angle distribution must be considered. Figure IV-14 shows the momentum relaxation distance as a function of energy for impurity scattering and for the polar optical phonons. Notice that the doping density has a pronounced effect on the momentum relaxation distance.
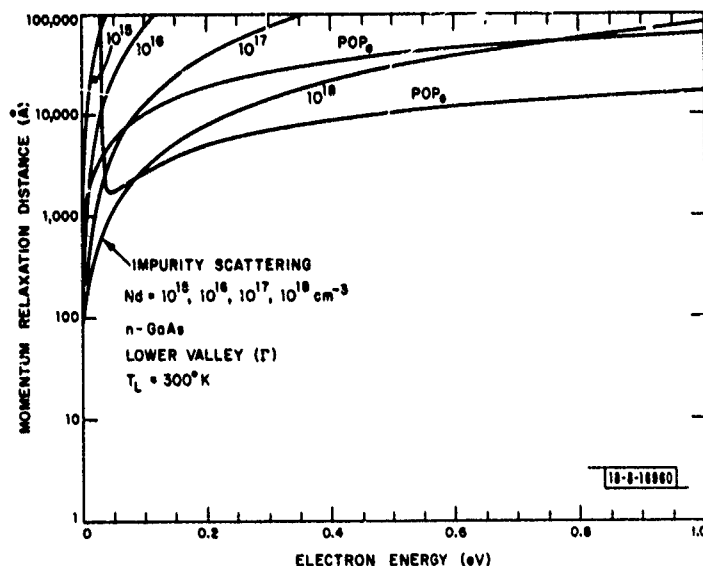
Fig. IV-14. The momentum relaxation distance for polar optical phonons and impurity scattering in the lower valley for GaAs.

The basic scattering mechanisms can now be averaged over an electron distribution function, such as a displaced Maxwellian, and used in device modeling equations. The most useful parameters for device modeling are the energy and momentum relaxation times which can be easily calculated from the mean free paths, the phonon energies, and the scattering angle distribution functions. In general, the energy and momentum do not relax at the same rate, which leads to many important effects in small and high-frequency devices such as velocity overshoot.

M. E. Elta

REFERENCES

1. M. W. Geis, D. C. Flanders, and H. I. Smith, Appl. Phys. Lett. **35**, 71 (1979), DDC AD-A076745.

2. M. W. Geis, D. C. Flanders, H. I. Smith, and D. Antoniadis, J. Vac. Sci. Technol. **16**, 1640 (1979).

3. Solid State Research Report, Lincoln Laboratory, M.I.T. (1979:1), pp. 51-53, DDC AD-A073152.

4. W. L. Eversole, D. J. Mayer, P. W. Bosshart, M. deWitt, C. R. Hewes, and D. D. Buss, Intl. Solid State Circuits Conf. Digest of Technical Papers (February 1978), pp. 86-87.

5. Solid State Research Report, Lincoln Laboratory, M.I.T. (1979:4), pp. 29-31.

6. Ibid. (1977:1), p. 29, DDC AD-A041226/2.

7. S. M. Sze, Physics of Semiconductor Devices (Wiley, New York, 1969).

8. W. Fawcett, A. Boardman, and S. Swain, J. Phys. Chem. Solids **31**, 1963 (1970).

9. J. Ruch and W. Fawcett, J. Appl. Phys. **41**, 3843 (1970).

10. W. Fawcett and D. Herbert, J. Phys. C: Solid State Phys. **7**, 1641 (1974).

V. ANALOG DEVICE TECHNOLOGY

A. A SAW CHIRP-TRANSFORM SYSTEM FOR UPLINK DEMODULATION OF FSK SATELLITE COMMUNICATION SIGNALS

In certain satellite communication systems it is advantageous to demodulate many signals simultaneously on board the satellite. An example is the multiple uplinks from simultaneous users. A compact, low-power, high-speed satellite-borne uplink demodulator which exploits the capabilities of reflective-array compressors (RACs) configured as SAW chirp-Fourier-transform circuits to demodulate high-chip-rate frequency-shift-keyed (FSK) signals from a large number of users has been developed.

The demodulator is designed to process 4-ary FSK signals. In this mode each user is assigned a separate set of four frequencies and transmits on one of the assigned frequencies during each chip interval as determined by the desired information to be transmitted. Signals for successive chips are assumed to be incoherent. During each chip period, the demodulator must measure the energy in each of the four frequencies assigned to each user. These measurements are combined over several chips, and a maximum-likelihood symbol decision is made.

In the intended application, each of 100 users would employ 4-ary FSK modulation. The 400 possible frequencies have a 38-kHz spacing, thus covering an overall 15.2-MHz bandwidth. This chip period is 50 μsec. These parameters are well matched to the capacities of SAW RAC devices.[1]

The overall form of the chirp-transform[2-5] demodulator is shown in Fig. V-1. The system is a pair of convolve-multiply-convolve (C-M-C) circuits connected in parallel. The parameters of the individual RAC devices are summarized in Table V-1. Typical signals are indicated at several points in the circuit. The input is a sum of 50-μsec gated-CW signals. They are delayed according to their frequency by the differential delay (RAC 1), with the high frequencies delayed the least. An RF impulse is applied to the expander (RAC 2), and the expander output is a down-chirp waveform. This single down chirp is mixed with the delayed input signals to yield a series of down chirps in the lower sideband of the mixer output, one down chirp for each input signal. The down chirps all cover the same frequency band, but they are delayed in proportion to the input frequency. The down-chirp waveforms are compressed by the compressor (RAC 3) and produce a series of pulses, one for each input. The amplitude of each pulse is proportional to the amplitude of the corresponding input signal. The log of the compressed pulse envelope is sampled by a sample-and-hold A/D at times corresponding to the assigned frequencies. These samples are passed to the digital processor for chip combining and symbol decisions. It should be noted that the down chirp out of the expander is longer than the analysis time. It is therefore necessary to ping-pong two expanders to analyze 100 percent of the time.

In order to reject out-of-band interference, a bandpass filter is required at the demodulator input. Figure V-2 shows the amplitude response of the RAC device developed for use as the initial differential delay line shown schematically in Fig. V-1. The device has a very square bandpass response which is well matched to the band of desired frequencies. It is difficult to obtain a filter with as low a shape factor by other means. This feature of RAC devices has been previously exploited in a variable-bandwidth filter.[6] Thus, the differential delay line in Fig. V-1 serves two functions, bandpass filtering and dispersive delay. For measurement of spectral
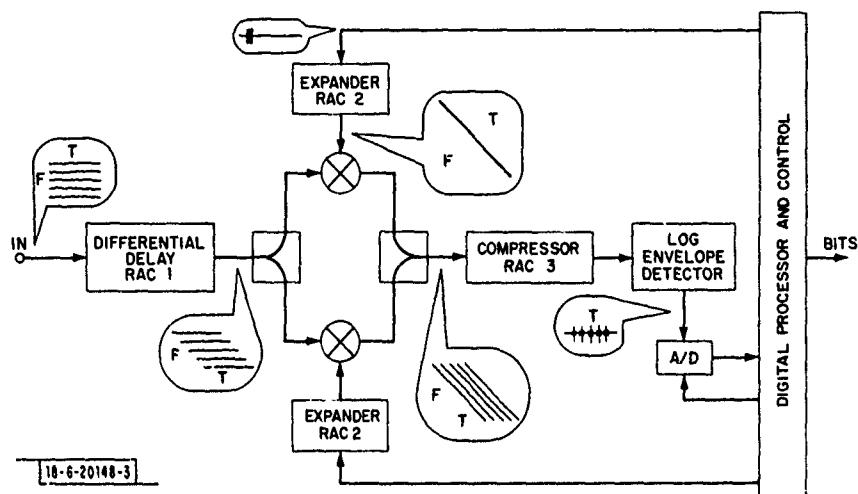
Fig. V-1.   FSK chirp demodulator using SAW devices.

TABLE V-1					
RAC PARAMETERS					
	Center Frequency (MHz)	Bandwidth (MHz)	Dispersion (μsec)	TB Product	Weighting
Differential Delay, RAC 1	100	15.2	33.6	511	Flat
Expander, RAC 2	250	37.8	83.6	3160	Flat
Compressor, RAC 3	150	22.6	50.0	1130	1.5 Kaiser-Bessel

Fig. V-2.   Amplitude response of differential delay line RAC.

46

power density, specifications on the phase response of this device are relatively loose. On the other hand, the RAC must have good triple-transit suppression to minimize intersymbol interference.

In the C-M-C configuration, weighting (windowing) for sidelobe suppression may be incorporated in the compression filter. Thus, this de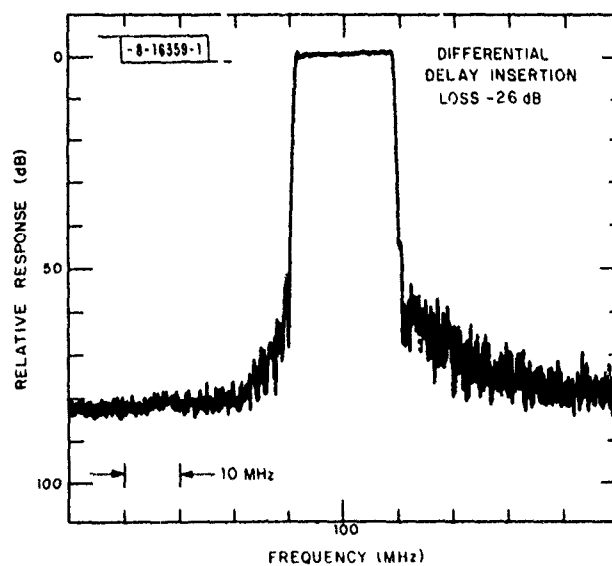vice also serves a dual function. Typical phase errors in RAC devices yield a structure of near-in sidelobes which is accurate down to a level about 35 dB below the mainlobe. This is adequate for the intended application. Furthermore, RAC devices yield particularly good suppression of far-out sidelobes, an important consideration in reducing crosstalk in a nearly filled band of frequencies.
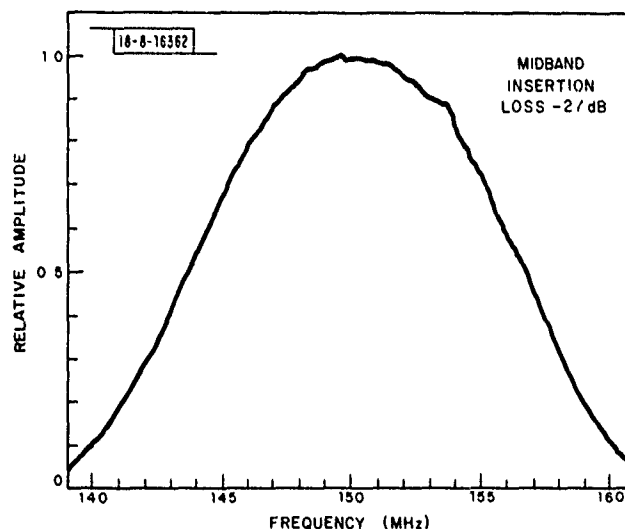

Fig. V-3. Amplitude response of RAC compressor.

The first series of RAC devices has been fabricated, individually evaluated, and inserted in a preliminary version of the actual electronic system. Figure V-3 shows the weighted amplitude response of the RAC compressor. The response is quite close to the specified Kaiser-Bessel weighting. The response of the differential delay line was shown in Fig. V-2. The first cut at the expander design yielded devices with a response that was slightly tilted (<2 dB) across the operating band. Prior experience with RAC devices indicates that, with further design interations, increasingly improved phase and amplitude response will be achieved in subsequent devices.

The crosstalk performance of the demodulator is directly related to the choice of window function[7] and the phase and amplitude accuracy of the RAC devices. The precision of these devices yields good overall performance. A preliminary result is shown in Fig. V-4. Here a single test frequency is entered, and the output of the SAW chirp transform is displayed on an oscilloscope. Figure V-4 demonstrates the ability of the demodulator to suppress far-out sidelobes. This ability of a RAC device to suppress far-out sidelobes is enhanced by a geometric effect.[8] "Squared-off" reflector arrays add cosine-squared tails to the initial Kaiser-Bessel weighting on the RAC groove depth, thus yielding a significant reduction of far-out sidelobes as compared to a sharply truncated Kaiser-Bessel impulse response. A few microseconds away
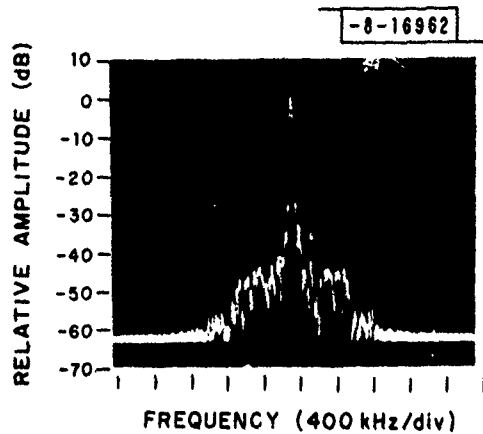
47

Fig. V-4. Main output pulse and far-out sidelobes for a single gated tone processed by the FSK demodulator.

Fig. V-5. Main pulse and near-in sidelobes obtained for the same conditions as in Fig. V-4.
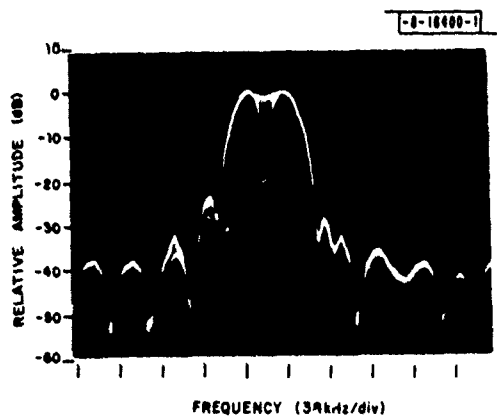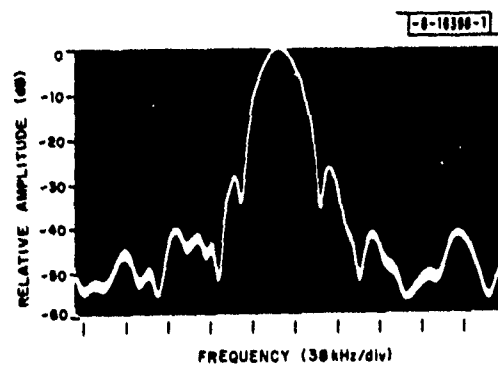

Fig. V-6. Output of logarithmic amplifier for two equal-amplitude signals with a frequency separation of 38 kHz.

from the main pulse (corresponding to approximately 10 adjacent possible FSK frequencies) the sidelobes fall off rapidly to a level below −60 dB. The display is limited by the dynamic range of the logarithmic amplifier. Figure V-5 shows the character of the near-in sidelobes, which are within a few decibels of the theoretical value for the Kaiser-Bessel window employed.

The ability of the demodulator to measure the spectral energy at closely spaced frequencies is shown in Fig. V-6. Here two equal-amplitude signals separated by the specified spacing of 38 kHz are processed by the demodulator. At the peak of each of its corresponding outputs, the measured spectral energy for one signal is relatively unaffected by the presence of the adja-
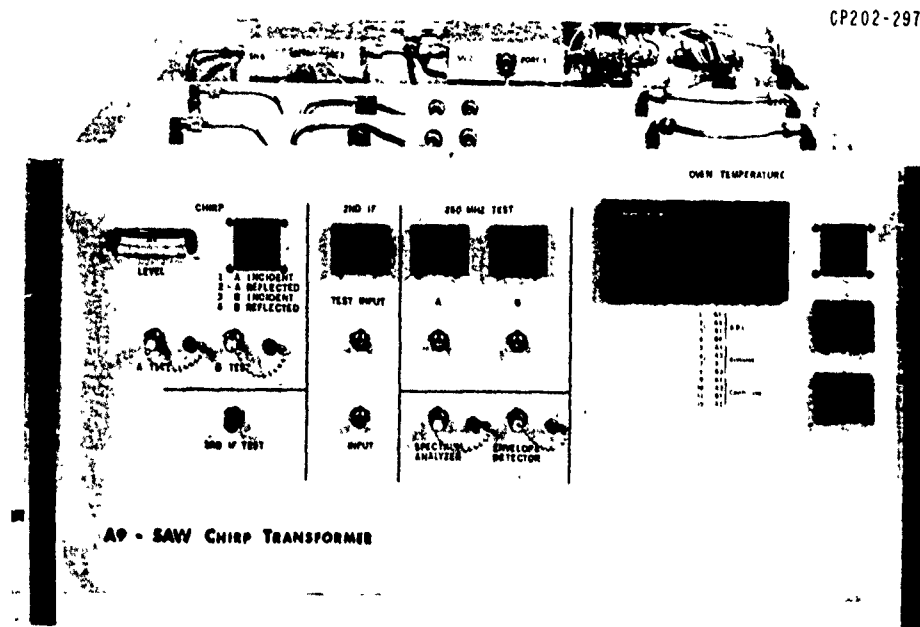

Fig. V-7. The brassboard SAW chirp transform system.

A weight- and power-efficient FSK demodulator, shown in Fig. V-7, has been designed which takes advantage of the characteristics of SAW chirp-Fourier-transform circuits to process high-data-rate signals from 100 simultaneous users. The demodulator incorporates data windowing, which provides substantial rejection of inter-user crosstalk. The capabilities of the demodulator are likely to have a major effect on the design of future satellite-communications systems.

V. S. Dolat R. R. Rhodes (Group 69)
R. C. Williamson D. M. Boroson (Group 69)

B. WIDE-BANDWIDTH ACOUSTOELECTRIC CONVOLVERS

The use of the high-performance acoustoelectric convolvers as programmable matched filters[9,10] provides a large instantaneous signal bandwidth and allows the encoding waveform to be changed from bit-to-bit. The changing waveform, in turn, provides resistance to repeat jamming, enables secure communications and yields improved performance in the presence of multipath. This report presents (1) the results on shock and vibration tests performed on gap-coupled acoustoelectric convolvers,[11] (2) results on convolvers with input bandwidths of 200 MHz,[11] and (3) projections on the range to which acoustoelectric convolver performance can be extended.[12]

TABLE V-2

VIBRATION TESTS* OF DPSK ACOUSTOELECTRIC CONVOLVER

(a) CW Vibration Test

Vibration Frequency Range	5 to 2000 Hz
Maximum Acceleration	10 g
Time Duration	3 hr/axis, 3 axes

(b) Random Vibration Test

Vibration Frequency Range	15 to 2000 Hz
RMS Acceleration	16.4 g
Time Duration	1 hr/axis, 3 axes

(c) Shock Test

Maximum Acceleration	40 g
Shock Time Duration	11 msec
Number of Shocks	6 shocks/axis, 3 axes

*These tests are consistent with military standard for aircraft, jeep, and tracked-vehicle equipment.
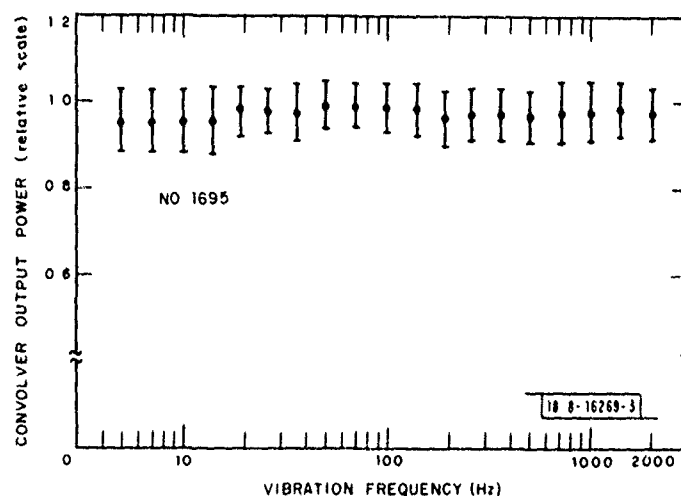

Fig. V-8. Acoustoelectric convolver performance during CW vibration test.

1. Shock and Vibration Tests

The basic structure of the acoustoelectric convolver developed at Lincoln Laboratory[10] consists of a lithium niobate ($LiNbO_3$) delay line separated from two narrow silicon strips by an air gap of about 0.45 μm. An array of rails[13] which have been ion-beam milled into the surface of the $LiNbO_3$ supports the silicon. A unique mechanical structure employing a series of beryllium-copper springs maintains a gap uniformity of ±0.02 μm over a wide temperature range. The structural ruggedness of these devices has recently been demonstrated by a series of dynamic shock and vibration tests on a convolver having a silicon interaction length of 22 μsec (7 cm) (Ref. 10). These tests are consistent with military specification (MIL-STD-810C) for aircraft, jeep, and tracked-vehicle radio equipment. The dynamic tests, which consisted of (a) a CW vibration test, (b) a random vibration test, and (c) a shock test, are summarized in Table V-2. Input and reference signals at levels of +7.5 and +18 dBm, respectively, were used for the dynamic tests. The signals were pseudonoise (PN) encoded with 1024 chips/11-μsec bit. The correlation peak of this PN code was monitored at the convolver outputs throughout the tests. Figure V-8 is a plot of the convolver output power vs CW vibration test frequency. No serious degradation was observed during the dynamic tests. In addition, the frequency response and interaction uniformity of the device were measured before and after the dynamic tests, and no degradation was observed.

2. 200-MHz Bandwidth

To achieve the 200-MHz convolver bandwidth, delay lines with center frequency of 500 MHz and fractional bandwidth of 40 percent are employed. The delay line insertion losses, measured at 500 MHz, are 27.5 and 32.5 dB, respectively, before and after the silicon is mounted. The conversion efficiency, or F-factor, is used for convolvers in the same sense as for mixers and other parametric devices. Plotted in Fig. V-9 are the F-factors of the two convolver outputs (ports 3 and 4) and the sum (Σ) of the two through a 0° to 180° hybrid as functions of frequency for gated-CW inputs. All of these outputs reflect a 3-dB input bandwidth of 200 MHz. The F-factor out of the sum port is −77.5 dBm at 500 MHz, which is in very good agreement with the theoretically predicted value of −77 dBm. Also, the F-factor measured at a temperature of 60°C is only degraded 1.5 dB with respect to the F-factor at room temperature, a temperature insensitivity that is predicted by theory.
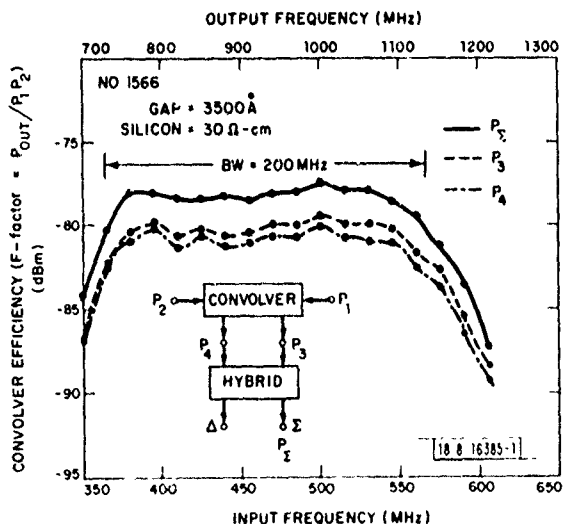
Fig. V-9. Output frequency response of wideband convolver. The two output ports are labeled P_3 and P_4 while the sum port of the 0° to 180° hybrid is labeled P_Σ.

CONVOLVER

P_2 o— —o P_1

P_4 P_3

HYBRID

1 dB

Δ Σ
P_Σ

P_Σ (dBm)

−40

−50

−60

−70

−80

−88

DYNAMIC RANGE = 46 dB

NO 1566
500 MHz

THERMAL NOISE FLOOR

10   20   30   40

$$10 \log \left[\frac{P_1 P_2}{(1\,mW)^2} \right] (dBm)$$
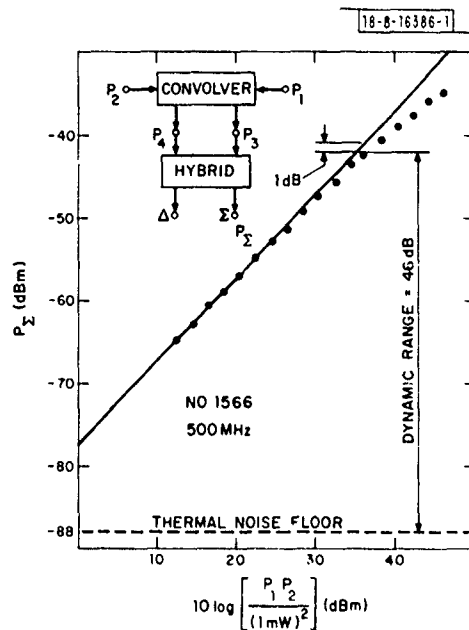
Fig. V-10. Convolver output power (P_Σ) vs product of the input powers.

10 mV   500 444

500 MHz   1 uS

(a)

10 mV   500 468

500 MHz   1 uS
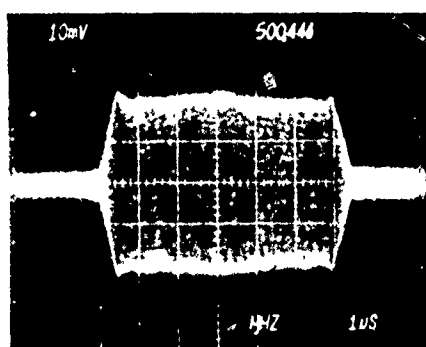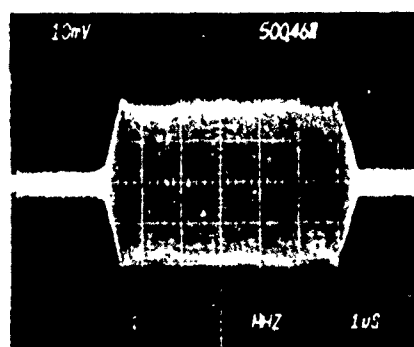
(b)

Fig. V-11. Interaction uniformity of wideband convolver for (a) port 3 and (b) port 4.

The total output power of the convolver as a function of input power levels is shown in Fig. V-10. The output power P_Σ in decibels above 1 mW is plotted as a function of the sum of the two input power levels P_1 and P_2. The two inputs were equal in power during this measurement. Note that the output is linear with input power up to levels of +18 dBm, at which point 1-dB compression in the F-factor is observed. The output power at the 1-dB compression point is −42 dBm. A dynamic range of 46 dB above kTB is observed. However, as indicated by Fig. V-10, the saturation is soft and a higher compression point may be acceptable in certain applications.

The CW self-convolution spurious output is down 35 dB from the actual convolution. This is consistent with the expectation that the suppression in CW self-convolution is approximately equal to the delay line loss of the device. Uniformity scans of the two interaction regions are shown in Fig. V-11. Notice that the amplitude fluctuates by less than ±1/2 dB. The designed and measured values of the convolver characteristics are summarized in Table V-3.

TABLE V-3 CHARACTERISTICS OF WIDE BANDWIDTH ACOUSTOELECTRIC CONVOLVER		
	Expected	Measured
Bandwidth	200 MHz	200 MHz
Interaction Length	12 μsec	12 μsec
F-Factor	−77 dBm	−77.5 dBm
Interaction Uniformity	±1.0 dB	±0.5 dB
Maximum Output Power*	−41 dBm	−42 dBm
Dymanic Range†	47 dB	46 dB
F vs Temperature (20/60°C)	−77/−78.5 dBm	−77.5/−79 dBm
Input and Output VSWR	<5:1	<6:1
Input/Output Isolation	>60 dB	≥60 dB
Output/Output Isolation	>30 dB	≥40 dB

* Convolver output power at 1-dB compression.

† Maximum convolver output power vs thermal noise floor at −88 dBm.

3. Device Projections

While the current DPSK convolver provides impressive signal-processing performance,[10,11,13] it is worthwhile to project the range to which device performance can be extended. In considering the limitations in convolver performance, the following two figures of merit usually are sufficient for determining system applicability: (a) processing gain, which is ideally equal to the time-bandwidth product and (b) dynamic range, which is the difference between the maximum output power and the thermal noise floor (or the maximum spurious level).

In designing acoustoelectric convolvers there are clear trade-offs between the fractional bandwidth, center frequency, and interaction length. The internal efficiency factor M is inversely proportional to both operating frequency and interaction length. Additional loss in the output circuit can be incurred when the electromagnetic length of the silicon is greater than one-quarter wavelength at the output frequency. For devices having short to moderate processing times, the maximum output power is determined by the saturation level of the nonlinear mixing interaction in the silicon. In this region, the acoustic efficiency of the SAW delay line may not directly affect the device dynamic range. On the other hand, for devices having relatively long processing times the maximum output power is often limited by acoustic saturation of the SAW delay line; here the device dynamic range is limited by both the delay line response and overall conversion efficiency (F-factor). Based on the theoretically predicted convolver performance (which has been proven to agree within 2 dB with measured data for a wide range of devices) along with the measured data on the saturation levels up to 500 MHz and their extrapolation beyond 500 MHz, a time-bandwidth plot of projected air-gap coupled acoustoelectric convolver performance along with some experimental data points is constructed in Fig. V-12. This chart
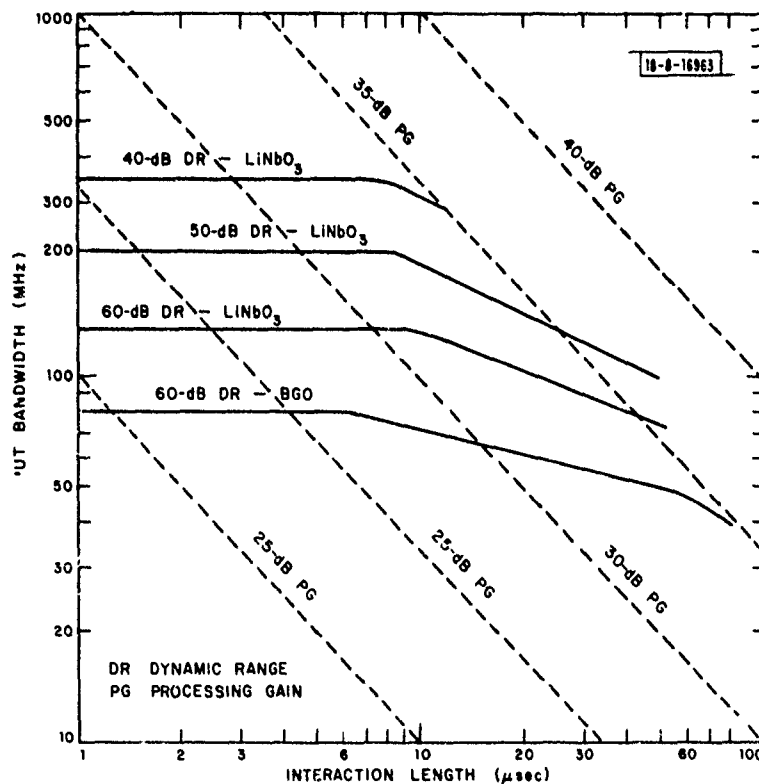
Fig. V-12. Time-bandwidth limitations of acoustoelectric convolvers.

is useful in projecting potential device application. Maximum fractional bandwidths of 45 percent were assumed for the devices with lithium niobate delay lines and 15 percent for the devices with bismuth germanium oxide (BGO) delay lines. A fractional bandwidth of 48 percent (at an input center frequency of 500 MHz) was recently demonstrated with a Si-LiNbO$_3$ convolver.

REPORT DOCUMENTATION PAGE	READ INSTRUCTIONS BEFORE COMPLETING FORM	
1. REPORT NUMBER ESD-TR-79-325	2. GOVT ACCESSION NO. AD-A089 822	3. RECIPIENT'S CATALOG NUMBER
4. TITLE *(and Subtitle)* Solid State Research, 1980: 1.	5. TYPE OF REPORT & PERIOD COVERED Quarterly Technical Summary rept. 1 November 1979 – 31 January 1980	
	6. PERFORMING ORG. REPORT NUMBER 1980:1	
7. AUTHOR(s) Alan L. McWhorter	8. CONTRACT OR GRANT NUMBER(s) F19628-80-C-0002	
9. PERFORMING ORGANIZATION NAME AND ADDRESS Lincoln Laboratory, M.I.T. P.O. Box 73 Lexington, MA 02173	10. PROGRAM ELEMENT, PROJECT, TASK AREA & WORK UNIT NUMBERS Program Element No. 65705F Project No. 649L	
11. CONTROLLING OFFICE NAME AND ADDRESS Air Force Systems Command, USAF Andrews AFB Washington, DC 20331	12. REPORT DATE 15 February 1980	
	13. NUMBER OF PAGES 72	
14. MONITORING AGENCY NAME & ADDRESS *(if different from Controlling Office)* Electronic Systems Division Hanscom AFB Bedford, MA 01731	15. SECURITY CLASS. *(of this report)* Unclassified	
	15a. DECLASSIFICATION DOWNGRADING SCHEDULE	

16. DISTRIBUTION STATEMENT *(of this Report)*

Approved for public release; distribution unlimited.

17. DISTRIBUTION STATEMENT *(of the abstract entered in Block 20, if different from Report)*

18. SUPPLEMENTARY NOTES

None

19. KEY WORDS *(Continue on reverse side if necessary and identify by block number)*

solid state devices	photodiode devices	infrared imaging
quantum electronics	lasers	surface-wave transducers
materials research	laser spectroscopy	charge-coupled devices
microelectronics	imaging arrays	acoustoelectric devices
analog device technology	signal processing	

20. ABSTRACT *(Continue on reverse side if necessary and identify by block number)*

This report covers in detail the solid state research work of the Solid State Division at Lincoln Laboratory for the period 1 November 1979 through 31 January 1980. The topics covered are Solid State Device Research, Quantum Electronics, Materials Research, Microelectronics, and Analog Device Technology. Funding is primarily provided by the Air Force, with additional support provided by the Army, DARPA, Navy, NASA, NSF, and DOE.

The processing times were limited to 50 μcc (80 μsec), which is consistent with LiNbO$_3$ (BGO) substrates having a maximum length of 8 (6) in. From this projection, we find that an acousto-electric convolver with a processing gain of 37 dB and a dynamic range of 50 dB can be realized. Because of their compactness, ruggedness, and signal-processing power, convolvers will likely find wide application in future spread-spectrum communication systems.

I. Yao
S. A. Reible

REFERENCES

1. R. C. Williamson, "Properties and Applications of Reflective-Array Devices," Proc. IEEE 64, 702-710 (1976), DDC AD-A028461/2.

2. V. S. Dolat, M. B. Schulz, L. A. Veilleux, G. R. McCully, and R. C. Williamson, "High-Performance Hybrid SAW Chirp-Fourier-Transform System," in 1978 Ultrasonics Symposium Proceedings (IEEE, New York, 1978), pp. 527-532, DDC AD-A069933/0.

3. C. Lardat, "Improved SAW Chirp Spectrum Analyzer with 80 dB Dynamic Range," ibid., pp. 513-521.

4. O. W. Otto, "The Chirp Transform Signal Processor," in 1976 Ultra-sonics Symposium Proceedings (IEEE, New York, 1976), pp. 365-370.

5. M. A. Jack and E. G. S. Paige, "Fourier Transformation Processors Based on Surface-Acoustic Wave Chirp Filters," Wave Electronics 3, 229-247 (1978).

6. J. Melngailis and R. C. Williamson, "Filter with Bandwidth Continuously Variable from 5 to 100 MHz," in 1977 Ultrasonics Symposium Proceedings (IEEE, New York, 1977), pp. 965-968.

7. L. S. Metzger, D. M. Boroson, J. J. Uhran, Jr., and I. Kalet, "Receiver Windowing for FDM-MFSK Signals," IEEE Trans. Commun. COM-27, 1519-1527 (1979).

8. R. C. Williamson, V. S. Dolat, R. R. Rhodes, and D. M. Boroson, "A Satellite-Borne SAW Chirp-Transform System for Uplink Demodulation of FSK Communication Signals," in 1979 Ultrasonics Symposium Proceedings (IEEE, New York, 1979), pp. 741-747.

9. J. H. Cafarella, J. A. Alusow, W. M. Brown, and E. Stern, "Programmable Matched Filtering with Acoustoelectric Convolvers in Spread-Spectrum Systems," in 1975 Ultrasonics Symposium Proceedings (IEEE, New York, 1975), pp. 205-208, DDC AD-A031716/4.

10. S. A. Reible, J. H. Cafarella, R. W. Ralston, and E. Stern, "Convolvers for DPSK Demodulation of Spread Spectrum Signals," in 1976 Ultrasonics Symposium Proceedings (IEEE, New York, 1976), pp. 451-455, DDC AD-A040519/1.

11. I. Yao and S. A. Reible, "Wide Bandwidth Acoustoelectric Convolvers," in 1979 Ultrasonics Symposium Proceedings (IEEE, New York, 1979), pp. 701-705.

12. R. A. Becker, S. A. Reible, and R. W. Ralston, "Comparison of Acousto-electric and Acoustooptic Signal Processing Devices," in Optical Signal Processing for C^{3}I Proceedings, Vol. 29 (SPIE, Bellingham, WA, 1980), pp. 126-133.

13. S. A. Reible, K. L. Wang, and V. S. Dolat, "Transverse Modes in Acoustoelectric Convolvers," in 1978 Ultrasonics Symposium Proceedings (IEEE, New York, 1978), pp. 48-53, DDC AD-A069929/8.

END

DATE
FILMED

11-80

DTIC